A hidden component of magnetic storms makes Earth's mantle transition zone look drier than it is

Seokhoon Oh

Department of Energy and Resources Engineering, Kangwon National University, Chuncheon 24341, Republic of Korea

Corresponding author. Email: gimul@kangwon.ac.kr

Peer-review status. This is a non-peer-reviewed preprint submitted to EarthArXiv. The manuscript has been submitted to *Science* for peer review.

Contents. The main text is followed by the full Supplementary Materials in this single PDF.

Data and code. All processing and experiment code, locked intermediate archives, and the acceptance-gate ledger are deposited at Zenodo: https://doi.org/10.5281/zenodo.21184326. All input data are public (INTERMAGNET; WDC Kyoto Dst; SILSO; CHAOS-7).

Title: A hidden component of magnetic storms makes Earth's mantle transition zone look drier than it is

Authors: Seokhoon Oh[1]*

Affiliations:

[1]Department of Energy and Resources Engineering, Kangwon National University; Chuncheon 24341, Republic of Korea.

*Corresponding author. Email: gimul@kangwon.ac.kr

Abstract: Electromagnetic sounding provides a primary geophysical constraint on water in Earth's mantle transition zone, yet conductivity models disagree by up to an order of magnitude. We identify a source-side systematic invisible to internal consistency checks: omitting the degree-3 zonal (P_3^0) storm-field component biases transition-zone conductivity by 0.1–0.35 decades, a tenth to a quarter of that spread. The bias scales with network sparsity. The carrier is not power but phase: a storm-band component nearly anti-phase to the ring current. Injection reproduces the bias quantitatively; independent storm catalogs and null, shuffled-geometry, and network controls exclude artifacts. It maps to factors of 1.5–3.8 in water, 80–275 K, and 30% of the 660-km contrast. At the highest laboratory dry floors it becomes a dry/wet misclassification. Source co-estimation removes it.

Main Text:

Introduction

The mantle transition zone (410–660 km depth) can store as much water as the surface oceans, bound in the hydrous defects of wadsleyite and ringwoodite (*1–3*). A hydrous ringwoodite inclusion in diamond shows that at least locally it does (4). Whether it does in bulk is a first-order question for the evolution of Earth's oceans and plate tectonics. The principal geophysical window is electrical conductivity. Hydrogen dissolved in transition-zone minerals raises conductivity by orders of magnitude (*5–7*). Global conductivity models built from geomagnetic observatory and satellite records are therefore read, through laboratory calibrations, as water meters for the deep mantle.

Those models, however, disagree among themselves by up to an order of magnitude in the transition zone. Between two flagship satellite-era models alone the gap reaches 1.27 decades at 450–670 km (11, 13; SM §S2a), in part reflecting their different sensitivity bands. This spread is usually attributed to data coverage, regularization choices, and the laboratory calibration debate (*8–14*). The deepest assumption of the measurement itself has received less scrutiny. That assumption is that the source field driving the induction, dominated by the storm-time ring current, has the geometry of a single spherical harmonic, P_1^0 (*15, 16*). The assumption is historically motivated. Degree-1 does dominate the storm-time field (*15*), and the workhorse C-response is *defined* through it (*16*). For this reason its failure mode has stayed invisible. The error enters not through the dominant term but through what the dominant-term-only fit does with everything else. Classical long-period studies recognized higher zonal terms (*15, 17, 18*). Olsen (*17*) compared a single-P_1^0 and a source-aware treatment of the same observatory data. He already found the P_1^0 responses 'too high', with conductivity correspondingly underestimated, and attributed it to harmonics beyond P_1^0. Non-axisymmetric source structure has likewise been flagged as a nuisance for response estimation (*19, 20*). Yet a large fraction of the observatory-based literature, including single-station and regional C-response practice, still rests on the P_1^0-only assumption. The interpretation-scale penalty, the specific property of the source that controls it, and its dependence on network geometry have not been isolated.

Here we show that this assumption carries an interpretation-scale penalty, and we isolate its exact mechanism. In six years (2014–2019) of data from twelve mid-latitude observatories, omitting the storm-time P_3^0 term biases recovered transition-zone conductivity low by up to 0.35 decades. That is a tenth to a quarter of the inter-model spread, and it scales with network sparsity. We replicate this on an independent 15-year, 57-station archive (43 stations continuously operating) and on a century-scale, 130-observatory chain. The bias is carried by a specific, measurable property of the source. A storm-band P_3^0 component is phase-coherent with the main P_1^0 ring-current field and nearly anti-phase to it (measured phase $-157° \pm 12°$), with a coherent amplitude ratio of only ~4% at the discovery network. In-phase or randomly-phased components of the same power are nearly harmless. The anti-phase coherent component alone reproduces the full observed bias when injected into a synthetic Earth, and real station geometries drawn at random trace the same phase-selective transfer in both directions.

The consequence is that a single unmodeled source term can masquerade as a factor-of-two change in transition-zone water content. At the highest laboratory dry floors, this becomes a qualitative dry/wet misclassification. It can also appear as an 80–275 K thermal anomaly, or as a 30% change in the 660-km conductivity contrast that anchors the transition-zone water-filter debate. These are the quantities deep-Earth electromagnetic sounding exists to measure. The error is systematic, survives averaging, and is invisible to internal consistency checks. Both flagship models whose disagreement spans a representative published spread estimate their magnetospheric responses on the P_1^0 assumption (verbatim-verified; 11, 13, Table S6). But the bias is also diagnosable from the data themselves, predictable from a cheap coherence measurement, and removable by co-estimating source geometry with Earth structure. Its sign is fixed for the curated networks measured here. Correcting it therefore moves observatory-based water inferences in one direction, wetter, rather than merely widening their uncertainties. An unmodelled property of magnetic storms, the phase of their degree-3 zonal source field, thus distorts the electromagnetic image of the transition zone, measurably and removably.

Results

A half-decade bias and its single-term cure. Our reference chain performs spatial-domain source separation at every hourly epoch. This is followed by robust transfer-function estimation and regularized 1-D inversion (Materials and Methods). The P_1^0-only configuration of this chain is no strawman. It is the standard recipe of the C-response lineage: P_1^0 separation, robust response estimation, and smooth 1-D inversion (15, 26; Table S6). With it, the recovered conductivity profile falls 0.47 decades outside a three-profile representative benchmark over 400–900 km in the discovery band (periods ≥2 days). To calibrate what that distance means, we invert *exact* synthetic responses of each benchmark profile through the identical pipeline, using the same frequency bins, the same uncertainties, and the same regularization. This yields a machine floor of 0.12 decades, the unavoidable distance produced by parameterization and smoothing alone. The real-data excess of +0.35 decades is therefore a data-borne bias rather than an artifact of the metric (Fig. 1A,B; SM §S2).

Adding a single source term restores benchmark agreement. That term is the degree-3 zonal harmonic P_3^0, two coefficients in the epoch-wise separation. The recovered distance falls to 0.20, within a factor of two of the floor. It also raises transition-zone conductivity by 0.24 decades in the same-band paired comparison ($\Delta TZ \equiv \log_{10}\sigma[P_1^0{+}P_3^0] - \log_{10}\sigma[P_1^0\text{-only}] > 0$: the P_1^0-only chain underestimates conductivity). The shift is robust to the regularization choice (+0.24 to +0.27 over a ten-fold range of the smoothing weight, and equivalent under a depth-averaged metric; SM §S2). It also inflates the apparent 660-km conductivity jump by ×1.33 (from ×18.0 to ×13.6 in linear contrast; a 0.13-decade change). The response itself carries a diagnostic signature. With P_1^0 only, the real part of the transfer function is suppressed by a systematic 3–5% at 4–16-day periods (−3.4, −5.3, −4.6% at 4, 8, 16 days). The P_3^0 term removes this suppression (−1.3, −0.4, +4.7%; Fig. 1C).

The benchmark is a *representative* three-profile set used as the discovery-era internal anchor. Provenance is locked by reproducing the archived discovery inversion to all printed digits and the corrected model vector to better than 10^{-3} (SM §S2). The floor itself is anchor-dependent (0.10–0.26 per profile). This is one reason we report the paired transition-zone shift, an envelope-free quantity, as the headline measure throughout.

Two further facts frame the discovery. First, every internal quality metric *prefers the biased configuration*: misfit χ^2/n (0.25 versus 0.46), agreement between two independent estimators of the same data (8.6% versus 12.6%), and distance to published response *shapes* (8.8% versus 10.1%). An analyst auditing the biased chain with the field's standard toolkit would judge it the *better* chain by every internal indicator. Per-epoch leakage of the anti-phase internal degree-3 response into the apparent degree-1 pair produces a smooth, internally consistent transfer function that is nonetheless wrong. An isotropic 1-D Earth fits it comfortably (SM §S3). Second, we assemble the *actual* spread of published models here from author-released and free-access profiles (*11, 13, 46*). Both the biased and the corrected profiles lie comfortably inside it (SM §S2a). The bias hides within the literature's disagreement, invisible to external comparison as well as to internal checks, and amounts to 19–27% of that spread for this canonical sparse chain (9% at the densest network tested, below). Control configurations show the cure is specifically the true P_3^0 geometry, not extra freedom and not higher order (Fig. 1B; SM §S2). Were the improvement a regularization artifact, any extra column should help. Instead, P_3^0 bases at station-permuted coordinates (three seeds, identical degrees of freedom, pattern correlations up to $|r| = 0.69$) leave the benchmark unrestored and the chain biased like P_1^0-only (transition-zone deviations −0.21 to −0.34, outside the ±0.09 estimator-noise band). Conversely, escalating the basis with (3,±1) or (5,0) terms collapses the separation at twelve stations (condition numbers 1284 and 200). With sparse networks the usable source space is small and must be spent on the right harmonic.

The carrier is phase, not power. Why does so small a term matter? The recovered P_3^0 coefficient series has a storm-window amplitude of only 7% of the main field, and its overall correlation with the ring-current index is near zero (−0.07). Resolving this paradox is the central physical result of this study (Fig. 2). We decompose the P_3^0 series against P_1^0 in the storm band (4–16 days). This reveals a coherent component of amplitude ratio 0.036 ± 21% at phase −157° ± 12°, consistent with pure anti-phase within 2σ (deviation 23°, 1.9σ). A rotation, if real, would signature local-time structure of the current system. The sign is that expected from the classical multipole expansion of an equatorial ring current (*21, 22*), whose P_3^0/P_1^0 coefficient ratio for a thin equatorial loop is negative with magnitude $(a/b)^2/2$. The amplitude is of the expected order. The coherent amplitude corresponds to a ring-current distance $b \approx 3.7\, R_\mathrm{E}$ and the total amplitude to $b \approx 2.7\, R_\mathrm{E}$, both within observed storm-time ranges (*22*). The remaining ~half of the P_3^0 power is incoherent and, for the induction bias, largely irrelevant.

The carrier is measured by two independent routes that agree to 0.3%: a spectral cross-estimate at 4–16 days and a time-domain storm-window projection (Materials and Methods). Its amplitude is no artifact of estimation noise. Run on a synthetic with *no* degree-3 source and realistic colored noise, the full chain manufactures a spurious storm-window ratio of only 0.012, against 0.070 measured, a 5.8-fold excess (SM §S4).

We demonstrated the mechanism by controlled injection into a synthetic Earth. That Earth was driven by the real separated source waveforms, station geometry, gaps, and block-bootstrap residual noise (Materials and Methods; SM §S4–S5). Injection amplitudes are calibrated on the measurement's storm-window ratio, so the native-amplitude run is, by construction, the real operating point. The degree-3 induction uses the same forward operator's degree-3 kernel. Its weaker response (Re $Q_3 = 0.26$ versus Re $Q_1 = 0.32$ at 16 days) supplies the contrast that leakage converts into bias. Four waveform variants separate amplitude from phase. (i) Injecting the *measured* P_3^0 waveform at its native amplitude reproduces 82–90% of the observed transition-zone shift (+0.195 noise-free; +0.215 median under colored noise) and the bin-level signature. (ii) Injecting a *purely in-phase* P_3^0 of the same amplitude produces a bias of the *opposite sign* (−0.48 at the native ratio): the response real part is enhanced rather than suppressed. (iii) A randomly-phased, storm-by-storm component of the same power produces almost nothing (≤0.04 decades). (iv) The *anti-phase coherent* *limit*, evaluated at the independently measured coherent amplitude of 0.036, reproduces the observed bias to within its uncertainty (×1.01 ± ~0.2). Across the sweep the transfer is linear in the coherent amplitude, with $\Delta\mathrm{TZ} \approx +2.9\alpha$ for the measured waveform and $\mp 7\alpha$ for the in/anti-phase limits, and it is sign-selected by phase. This is a mechanism, not a curve fit (Fig. 2A). The recovered coefficients track the injected truth with correlation ≥0.999 and unit slope across the sweep (Fig. 2D), so the corrected configuration measures, rather than manufactures, the carrier.

The pathway is geometric. At the twelve-station network, projecting the (3,0) patterns onto the degree-1 basis shows the *internal* degree-3 response folding onto the apparent *external* degree-1 channel with coefficient +0.97 (SM §S5). An anti-phase internal n=3 field therefore masquerades as a weakened apparent induction response, that is, as a less conductive mantle. The degree-3 kernel's weaker response ($Q_3 < Q_1$) sets the conversion. The ~18% shortfall of the measured-waveform injection against the observed shift bounds, within this diagnostic, the contributions of Earth-model differences and of any non-P_3^0 structure that the (3,0) term absorbs in the real data.

A recurrent, storm-time component, independently confirmed. Five families of controls establish that this is a property of the storm source. They rule out an origin in our processing (Fig. 3; SM §S4–S8).

(i) Null and shuffled-geometry controls. The null synthetic is matched to the real operating point: a five-layer truth Earth, the *real* separated degree-1 waveforms preserving true storm timing, spectra, and activity, the real stations, gaps, and outages, and the real fit residual re-injected by block bootstrap. This truth contains *no* degree-3 source. On it, opening the P_3^0 degree of freedom moves the recovered transition zone by only −0.014 (range −0.023 to +0.002 over twelve realizations). The real-data effect (+0.239) lies outside every null realization, with opposite sign. Both configurations recover the synthetic truth at the oracle floor. Realistic colored noise is essential here. Matching it as independent Gaussians overstates the null variance nineteen-fold (SM §S4).

(ii) Independent storm selection. We also selected storm windows from the final Kyoto Dst index (*23*) instead of from our own data (73 events with only 66% window overlap). This reproduces the carrier at ×0.99. That route is independent of the spectral estimate (×1.01; Fig. 2A), so it closes the circularity that affects any self-selected storm analysis. The separated main-field series itself correlates with the independent index at 0.82 hourly and 0.98 in the storm band (Fig. 3A).

(iii) Recurrence, with episodic energy. The carrier is not a single-event accident. The five most energetic storms contribute only 9% of the coherent cross-power, and removing them *strengthens* the aggregate. Every leave-one-storm-out estimate preserves sign within 17%, and per-storm sign consistency is 75% across the 24 strongest events. Main-phase and recovery-phase projections are both anti-phase (−0.037, −0.043). A zero-coupling surrogate (circular shifts of the P_3^0 series) never reaches the measured coherence in 300 trials. Stratifying storms by independent intensity (minimum Dst), the coherent ratio is weakest in the largest storms (−0.023 in the strongest tercile versus −0.052/−0.053). This is consistent with asymmetric partial ring currents diluting the axisymmetric geometry. Quiet-time stratification is non-monotonic, leaving an ionospheric leak as the candidate for the small quiet-time residue, while storm-time local-time-fixed (ionospheric) channels are excluded directly by a disturbance local-time template test (SM §S7). The *energy* of the bias, however, is episodic. Storm-rich years carry it (+0.31), while storm-poor years are consistent with zero (−0.07 against a masking-noise floor of ±0.09). This is a direct warning for records and epochs of differing activity. The same masking experiments quantify an estimator-noise floor that recurs throughout this study. At six-year record length, single-storm-level attribution of the *inversion output* sits at the noise of segment recomposition ($\sigma \approx$ 0.09–0.10), while the carrier projection, with jackknife variation of 17%, is the precise instrument.

(iv) Network robustness. The carrier survives every single-station deletion (12/12 negative, ≤35% variation). It also survives an inland-only network (ocean induction excluded: carrier −0.037, shift +0.19) and the re-

moval of the two stations with the worst local-field residuals. Across the jackknife the carrier-predicted bias tracks the measured ordering ($r = +0.65$), while the amplitude scatter is estimator-noise dominated. The identifiability resource is latitude coverage rather than station count. Latitude-half subnetworks fail to separate the zonal degrees at all (condition numbers 313–1207), whereas longitude halves preserve the carrier sign.

(v) Independent archive and the network dose-response. We repeated the comparison on an independent 15-year, 57-observatory archive (2010–2024; 43 stations retained by a continuity filter). It replicates in sign: paired shift +0.11 (+0.14 era-gated), carrier −0.011 outside its no-coupling null, and a Dst-selected catalog of 188 events reproducing the carrier at ×1.4. The mechanism transfers quantitatively. Geometric leakage and the injection-calibrated transfer slope scale down together from the 12- to the 43-station network (+0.97 → +0.78 and 6.9 → 5.5 per unit carrier). A 2×2 attribution grid over matched epochs shows the amplitude change is carried by the *network*, not the period. The 9-, 12-, and 43-station networks give shifts of +0.33, +0.24, and +0.11 decades with carriers −0.040, −0.034, and −0.007. Random identifiable subnetworks resolve the full structure (Fig. 4). Sparse draws are a geometry lottery: twelve-station geometries span −0.6 to +0.4 decades, a 16–84% width of 0.8, collapsing to ±0.03 by thirty stations. The draws align along the phase-selective transfer in *both* branches. They include an in-phase geometry (carrier +0.086) that, as the phase mechanism predicts, lands on the opposite-sign branch ($-0.63 \approx -7c$). The measured carrier therefore contains network-mediated aliasing of unresolved source structure. It is a per-chain exposure diagnostic, not a universal source constant. One sparse geometry is carrier-blind (coherence ≈ 0 yet a −0.5-decade shift, optimizer-verified), marking the diagnostic as necessary but not sufficient at pathological geometries (SM §S11). Two residuals accompany the replication. First, the archive's chain-index correlation degrades in its earliest and latest years (0.45 in 2010–2011, a known baseline-wander era, and 0.40 in 2020–2024, unattributed; interior years reach 0.90), which motivates the era-gated value. Second, at 43 stations the linear-coherent prediction recovers only half the measured shift (×0.52, against ×0.96 at the sparse network), indicating a non-coherent residual pathway whose relative weight grows as the coherent carrier shrinks. A third record closes the curve from above (Fig. 4A). On a century-scale archive of 130 observatories, era-gated to 1940–2020 (assembly and validation detailed in SM §S11, with chain code and locked intermediates in the deposit), adding the P_3^0 term shifts transition-zone conductivity by +0.135 ± 0.034 decades (4σ) while *improving* the chain misfit (χ^2/n 1.41 → 1.07), and a 96-station subset gives +0.126. Three independent records, with different data sources, station sets, eras, and internal-field treatments, thus agree on a common curated-network systematic of ≈ +0.13 decades: +0.24 ± 0.18 at twelve stations over six years, +0.11 ± 0.07 at forty-three over fifteen, and +0.135 ± 0.034 at 130 over eighty. Random subnetworks drawn from the century pool reproduce the lottery in extreme form. Validated draws reach $|\Delta TZ| = 0.65$ with draw-dependent sign, gate-failed draws reach 2.5–3.4 decades, and only 38% of random twelve-station draws pass pre-registered chain-validation gates at all. The controlling variable is geometric balance, not station count per se. Curated networks of any size sit near the convergent systematic, while random unbalanced subsets populate the envelope. A synthetic negative control through the same machinery, a world with no (3,0) source term, returns $|\Delta TZ| \leq 0.002$, excluding analysis false positives (SM §S11). Most historical observatory chains operate in the high-dispersion regime.

What the bias means for Earth. Because laboratory conductivity laws disagree in absolute calibration, we translate the bias through sensitivity parameters only. This brackets both laboratory schools and the mechanism mixing they imply (SM §S9). The fair-band bias of 0.24 decades corresponds to a factor 1.5–2.5 in inferred water content, or 80–190 K in temperature. The floor-corrected discovery-band excess of 0.35 decades corresponds to factors 1.8–3.8, or 117–275 K (Fig. 5). The raw envelope distance of 0.47 decades, before machine-floor correction, reaches ×6.0 and 370 K and is retained in the figure as a labeled provenance tier. These temperature shifts are comparable to the lateral variations that seismology infers for the transition zone (*25*). The translation uses only sensitivity parameters: the water-content exponent $r \in [0.6, 1.4]$ and activation enthalpies $H \in [0.9, 1.5]$ eV, spanning both laboratory schools. The disputed absolute prefactors therefore cancel in ratio form, and the numbers are robust to the calibration debate. These water factors are nonetheless *lower bounds*. An interpreter inverts $\sigma_{\text{total}} = \sigma_{\text{dry}} + \sigma_{\text{wet}}(C_w)$ for water content, and the bias factor $[(1-\rho)/(10^{-\Delta}-\rho)]^{1/r}$, with ρ the dry fraction of the true conductivity, *grows* with the dry floor, because the inversion divides by a floor-suppressed sensitivity (SM §S9, fig. S8). Where dry conduction supplies a third to a half of the true conductivity, as under the more conductive laboratory school's dry values (*6, 14*), the floor-corrected discovery-band bias can push the apparent conductivity below the dry floor altogether toward the upper end of that regime: a wet transition zone misread as dry (a lower bound; SM §S9). We do not re-adjudicate the laboratory debate. The point is that the data-side systematic compounds it multiplicatively. For networks that carry the anti-phase coherent component, the bias direction is fixed. This includes every curated configuration measured here; a random geometry that reverses the carrier reverses the sign (Fig. 4B). P_1^0-only chains *underestimate* transition-zone conductivity, hence underestimate water content and temperature. And the apparent 660-km conductivity contrast, the quantity that anchors arguments about layered versus whole-mantle water circulation (*24*), inflates by ×1.33 under the biased source model. Part of the apparent sharpness of the 660-km barrier is therefore instrumental, so source-corrected chains read the boundary as less sharp, weakening at the margin the electrical case for a strict transition-zone water filter. This sits within a published jump range that itself spans +0.9 to +1.9 decades (SM §S2a). Finally, the bias amounts to 19–27% of the actual spread among flagship published models for the canonical sparse chain (SM §S2a). This raises a testable proposition: a substantial part of the literature's disagreement may reflect source-geometry treatment rather than Earth. The prediction is falsifiable by meta-analysis. Sparse P_1^0-response chains should *scatter* with station geometry by amounts following the dose-response of Fig. 4, with the canonical mid-latitude configurations sitting low. The dispersion itself is a candidate component of the published spread.

Discussion

Three points deserve emphasis. First, the hazard is *phase-selected*. Total higher-degree source power is the wrong risk metric. Surveys of source complexity that report only amplitude ratios will miss the bias entirely. A cheap diagnostic avoids this: the storm-band coherent ratio c between the P_3^0 and P_1^0 channels, measurable from any multi-station dataset by the projection used here. It quantifies the exposure directly. Through the transfer function, it predicts the conductivity error before any inversion is run. The 15-year ensemble adds the operational caveats. The diagnostic is chain-specific, because it includes network-mediated aliasing. At pathological sparse geometries it is necessary rather than sufficient. The safe regime is the dense-network limit, which the dose-response of Fig. 4 quantifies.

Second, the structural lesson generalizes. Internal consistency cannot certify source assumptions, because a wrong Earth fitted to a wrongly separated source remains internally self-consistent. In our chain (Results), the biased model was both internally preferred and externally unremarkable against the published spread. External anchors of a different kind were essential at every stage: machine-floor calibration of benchmark distances, pre-registered acceptance gates with documented revisions, independent activity indices, and injection closure.

Third, the remedy is practical. The P_3^0 term costs two coefficients in the epoch-wise separation. It is identifiable with as few as twelve stations provided the network spans sufficient latitude (SM §S8), and it removes the bias without degrading any other metric. The dose-response also shows that network densification buys real protection. At forty-three continuously operating stations the residual bias is +0.11 decades. That is still a ×1.2–1.5 water-content factor, but it is a fraction of the sparse-network exposure. The century chain bounds the other end. At 130 curated stations the residual is +0.135 ± 0.034. Densification saturates near a factor-two reduction, and the systematic that remains is set by source-model completeness rather than station count. Beyond roughly fifty stations the only remedy is to model the term.

The findings translate into a four-step audit that any group can run on its own chain in hours: (1) separate with the P_3^0 term included and measure the storm-band coherent ratio c against the degree-1 channel; (2) verify it against a zero-coupling surrogate and an independent storm catalog; (3) predict the conductivity exposure from c through an injection-calibrated transfer; (4) compare the paired inversions and adopt the source-aware configuration if they differ. Every ingredient is standard.

The scope of the claim is explicit. The quantitative bias measured here belongs to the networks and epochs tested, up to 57 stations and 15 years, and to the zonal channel such networks identify. The dose-response of Fig. 4 bounds its scaling, and storm-rich epochs carry more of it. Flagship global models that already solve degree-1 and degree-3 jointly in the storm band, or that co-estimate source structure (8–11, 20, 26), are not directly implicated. The exposed population is the P_1^0-response lineage. This includes single-station and regional C-response practice. It also includes, notably, *both* flagship models whose disagreement spans a representative published spread, each of which estimates its magnetospheric responses on the P_1^0 assumption (verbatim-verified; 11, 13, Table S6). Any chain whose source parameterization under-resolves the anti-phase coherent component is likewise exposed. A small quiet-time coherent residue (~ -0.01) remains unattributed. It does not track the ring current and is a candidate ionospheric leak (SM §S7), and it is not the bias carrier. The phase and magnitude of the carrier are *consistent with* a classical equatorial ring-current expansion. Several questions remain open (SM §S11): event-level attribution to specific magnetospheric current systems, the characterization of carrier-blind geometries, and the degraded chain-index correlation of the earliest and latest archive years.

Looking forward, the same arithmetic that makes this bias dangerous also makes it an opportunity. Century-scale observatory archives are the only route to the 30-day–5-year periods that sense the lower mantle (*18, 27, 28*). They were recorded under sparse networks, where source-geometry freedom is largest and the coherent-carrier diagnostic is cheapest to apply. The dose-response curve measured here doubles as a design tool for that program. It converts a proposed station list into an expected exposure before a single inversion is run, and it identifies latitude span, not station count, as the binding constraint. Treating source geometry as an estimable part of the inverse problem, rather than an assumption, is a prerequisite for resolving deeper structure. This study suggests it is also a prerequisite for sharpening estimates of how much water the deep mantle holds.

Materials and Methods

Data and pre-processing. The discovery chain uses hourly means from 12 mid-latitude INTERMAGNET observatories (*29*). These span absolute geomagnetic latitudes 22°–52° (Table S4) and cover 2014–2019 (52,584 hours; availability 96.8%), computed from definitive one-minute data. We subtract the CHAOS-7 core field (*30*). Residual static crustal fields are absorbed by per-station median removal over each station's valid epochs. Quality control removes |residual| > 4000 nT and >500 nT/h spikes. Horizontal components are rotated to centered-dipole (epoch-2015 pole) coordinates. The replication archive comprises 57 observatories (2010–2024), cut to the CHAOS-7 validity range. Of these, 43 stations are retained by a ≥90% availability filter and processed by the identical frozen pipeline (SM §S11).

Epoch-wise source separation. At every hour t we fit external/internal coefficient pairs $\{\varepsilon, \iota\}$ for a spherical-harmonic source basis by weighted least squares across the network, with no time-domain processing. For a Schmidt quasi-normalized term $S = P_l^m(\cos\theta)\,\mathrm{trig}(m\phi)$ the observation equations are $X = (\varepsilon + \iota)\,\partial_\theta S$, $Y = -(\varepsilon + \iota)(\sin\theta)^{-1}\partial_\phi S$, $Z = (l\varepsilon - (l+1)\iota)S$, evaluated in dipole coordinates. Missing data are handled natively, an epoch being solved when ≥7 stations report (≥10 in the 43-station archive). The corrected basis is {(1,0), (1,1)c, (1,1)s, (3,0)}: eight coefficients from 24 X- and Z-equations (condition number 35.6). The biased reference omits (3,0). The (1,0) pair $(\varepsilon_1^0, \iota_1^0)$ is the induction channel used downstream in both configurations, so the paired comparison isolates the source model rather than the Earth model.

Forward operator. The 1-D induction response is computed from a self-contained finite-element operator rather than an analytic Earth. For harmonic degree l the internal poloidal scalar obeys a single radial equation with a Robin surface condition. That condition couples it to the external forcing ε(t) and to an insulating-core closure. The core skin depth is ~2 km at our longest periods, so a superconducting inner boundary is exact for the band used. Mass-lumped P1 finite-element discretization yields a generalized eigenproblem, whose modal superposition gives the impulse response $q(t) = Q_\infty\,\delta(t) - \sum_j \tilde{a}_j\, e^{-t/\tau_j}$ with $Q_\infty = l/(l+1)$. Because forcing and observation share the surface node, the driving-point structure makes every mode weight $\tilde{a}_j \geq 0$ *structurally*. This is the spherical counterpart of the non-negativity underlying D^+ theory (*32, 33*). Two analytic anchors calibrate the implementation. The DC sum rule is reproduced to a few parts in 10^8–10^6. The frequency response matches an independent thin-shell propagator oracle to a few parts in 10^6 across T = 10^2–10^7 s (1.1×10^{-6} for the degree-1 channel; both degrees used here verified in SM §S1, Table S1a), with second-order grid convergence. Because the data are hourly, generation, estimation, and inversion all use the *discrete-time* (zero-order-hold) transfer function of this kernel, so the hourly discretization gap (≤1.9% for T ≥ 4 d) cancels by construction. The same machinery supplies the degree-3 kernel used in the injection experiments. The operator is verifiable from the Supplement alone (SM §S1), with a full pedagogical derivation in a methods companion under review.

Transfer-function estimation. The complex ratio $\hat{Q}(T) = \hat{\iota}_1^0/\hat{\varepsilon}_1^0$ is estimated with a robust segment method designed for red spectra. The method combines four elements. First, first-difference prewhitening, whose identical filter cancels exactly in the ratio. Second, single-line discrete Fourier coefficients (line k = 8 per segment of length 8T, 50% overlap, Hann taper) (*36*). Third, iteratively reweighted Huber segment averaging. Fourth, leave-one-segment-out jackknife standard errors. Segments spanning gaps longer than 6 h are discarded. Six period bins spanning T = 4–137 days are retained. Shorter periods, dominated by the ionospheric daily variation, are excluded following standard practice (*15, 17*).

Inversion and machine-floor calibration. Profiles are eight-layer $\log_{10}\sigma(z)$ Occam-style inversions (*34*) with second-difference smoothing. The regularization weight λ is selected once by a $\chi^2/n \approx 1$ scan and frozen across every configuration, bootstrap, and experiment. Multi-start Occam solutions give ΔTZ = +0.269, +0.266, +0.240 for λ = 300, 1000, 3000 (a 12% spread over a ten-fold range), and +0.245 to +0.218 under an alternative depth-averaged metric. Sensitivity analyses use multi-start optimization after a single-start local-minimum artifact was identified and documented (SM §S2). Benchmark distance is the median recovered $\log_{10}\sigma$ lying outside a three-profile published envelope over 400–900 km. Because this metric has a nonzero floor even for in-envelope truth, we calibrate it by inverting *exact* synthetic responses of each anchor profile through the identical bins, errors, and λ. This gives floors of 0.098–0.255 (median 0.129). The real P_1^0-only distance of 0.469 therefore carries a net data bias of +0.346. Source-model configurations M0 (P_1^0-only), M1 (+P_3^0; adopted), M2 (+(3,±1)), and M3 (+(5,0)) are compared in one run. Alongside them we run three negative controls Mbad1–3 in which the (3,0) pattern is evaluated at station-permuted coordinates, preserving the eight-coefficient count and conditioning (cond ≈ 29) while destroying the physical geometry (Table S1).

Carrier measurement. Storm-band series are formed as $\mathrm{bp}(x) = \mathrm{MA}_{24}(x) - \mathrm{MA}_{480}(x)$, a filter with zeros at the daily harmonics and a passband of roughly 1–20 days. From $\hat{\varepsilon}_1^0$ we self-detect 49 storms (peak threshold 40 nT, ≥5-day separation) and define windows [−24 h, +120 h) about each peak. The time-domain carrier is the energy-weighted aggregate of per-storm regressions, $c_{\text{storm}} = \sum\langle e_3 e_1\rangle / \sum\langle e_1^2\rangle = -0.0338$ (storm-bootstrap 95% CI [−0.052, −0.017]). Its spectral counterpart is the variance-weighted complex mean of single-line cross-estimates at 4–16 days, $\bar{c} = 0.0337\,\angle -156.9^\circ$ (combined phase uncertainty ±12.2°). Per-storm sign consistency is 75% of the 24 strongest storms (82% of all).

Recurrence and estimator-noise floor. A superposed-epoch stack of the band-passed $\hat{\varepsilon}_3^0$ across the 49 storms shows the anti-phase waveform directly (Fig. 3C). Two resampling floors recur throughout the study and set what can and cannot be attributed. Carrier confidence intervals are storm-level bootstraps. Against these, the projection's 17% jackknife variation identifies it as the precise instrument. Inversion-level attribution, by contrast, sits at the noise of segment recomposition ($\sigma \approx 0.09$–0.10 at six-year record length), measured by masking placebos of equal data volume. Single-storm attribution of the *inversion output* is therefore deliberately avoided. The paired transition-zone shift and the carrier projection, not per-event inversion differences, carry every quantitative claim.

Null models and independent controls. Three null references bound spurious coupling. A zero-coupling surrogate circularly shifts $\hat{\varepsilon}_3^0$ by a random lag. This preserves autocorrelation and seasonality while destroying the cross-coupling. None of 300 surrogates reaches the measured coherence (empirical $p < 1/300$, 95% band [−0.0075, +0.0060]). A random-calendar placebo of 49 non-storm windows returns a weaker but same-signed −0.020, because sub-threshold recurrent activity carries the same relationship. The correct reading is a continuous source-geometry coupling enhanced ×2.9 in storms. Storm windows are also drawn, independently of our own data, from the final Kyoto Dst index (*23*), and solar activity is taken from the SILSO sunspot record (*31*).

Injection experiments. We establish the mechanism by controlled injection into a synthetic Earth. The truth is a five-layer profile driven by the *real* separated degree-1 waveforms at the real station coordinates and availability mask. Three noise families are used. The primary v1c re-injects the real M1-fit residuals by 2192-h block bootstrap, which preserves amplitude, colouredness, and inter-station correlation while destroying source alignment. It is tested against iid-Gaussian (v1) and 0.3-nT white (v0) alternatives. The null outcomes on this degree-1-only truth are those quoted in Results. We then add a degree-3 source with its own truth kernel ($Q_3 < Q_1$; at $T = 16$ d, $Q_1 = 0.320 + 0.052i$ versus $Q_3 = 0.255 + 0.100i$, the contrast that leakage converts into bias). This defines four waveform variants calibrated by the storm-window ratio $\alpha = |\varepsilon_3^0/\varepsilon_1^0|$: A, the measured $\hat{\varepsilon}_3^0$ rescaled (native $\alpha = 0.0699$); B and B$^-$, the in-phase ($+\alpha\varepsilon_1^0$) and anti-phase ($-\alpha\varepsilon_1^0$) coherent limits; and C, storm-windowed with random per-storm sign. Projecting the (3,0) patterns onto the degree-1 basis gives the leakage coefficient +0.97 that converts an internal degree-3 response into an apparent degree-1 change (SM §S5).

Consequence translation. Laboratory conductivity laws disagree in absolute calibration by ~0.5–1 decade at fixed water content and temperature (*14*). We therefore translate the bias through *sensitivity* parameters only, in which the disputed prefactors cancel in ratio form. Water content maps as $\Delta \log_{10} C_w = \Delta \log_{10} \sigma/r$, with the exponent $r \in [0.6, 1.4]$ bracketing both laboratory schools (*6, 7, 14*). Temperature maps as $\Delta T = \Delta \log_{10} \sigma \cdot \ln 10 \cdot k_B T^2/H$, with activation enthalpy $H \in [0.9, 1.5]$ eV and $T \in [1600, 1900]$ K (Table S5). This first-order translation is a *lower bound*. An interpreter actually inverts $\sigma_{\text{total}} = \sigma_{\text{dry}}(T) + A\,C_w^r$ for water. Writing $\rho \equiv \sigma_{\text{dry}}/\sigma_{\text{true}}$, the water-content bias factor is $F = [(1-\rho)/(10^{-\Delta}-\rho)]^{1/r}$. This reduces to $10^{\Delta/r}$ as $\rho \to 0$ but *grows* with the dry floor. The inversion divides by a floor-suppressed sensitivity, so a larger dry fraction amplifies rather than buffers the error (SM §S9, fig. S8). For $\rho \geq 10^{-\Delta}$ no water solution exists and the verdict flips to "dry" (thresholds $\rho \geq 0.58$, 0.45, 0.34 for $\Delta = 0.239$, 0.346, 0.469). The 660-km contrast translation uses the locked inversion vectors directly. The inter-model-spread and jump-range comparisons use the verifiable published profiles of §S2a.

Network dose-response and century import. The dose-response ensemble draws random subnetworks of the 15-year archive at $N = 9$, 12, 20, and 30 stations (eight draws each, plus the full 43). Two identifiability constraints learned from the structured subsets are applied: latitude span ≥25° and separation condition number ≤150. Storm windows are fixed from the full-network catalog for comparability, and rejected draws are counted and reported. Uncertainties on ensemble medians are 16–84% ranges over draws. Carrier confidence intervals are storm-level bootstraps. Estimator-noise floors for inversion-level resampling are measured by placebo masking of equal data volume. The century-archive points in Fig. 4 are imported, with sign convention aligned, from the locked outputs of the 130-station era-gated chain assembled, validated, and deposited with this paper (SM §S11). Its paired A/B uses the same epoch-wise separation and the same inversion grid.

Its 20-draw envelope carries pre-registered chain-validation gates (anchor deviation ≤25%, reduced misfit within [0.3, 3]), and its record-level standard errors supply the uncertainties quoted for the three-record concordance.

All experiments ran against pre-registered acceptance gates. Six gate revisions occurred, and each is documented with its reason, alongside the one optimizer artifact found and fixed during sensitivity analysis (SM §S10, §S2). Every numerical result and figure regenerates deterministically from the locked intermediate archives. The complete processing and experiment code, the locked intermediate archives, and the acceptance-gate ledger are deposited (Data and materials availability). End to end, the paper is reproducible from the public input data alone.

References and Notes

1. J. R. Smyth, β-Mg_2SiO_4: a potential host for water in the mantle? *Am. Mineral.* **72**, 1051–1055 (1987).
2. D. L. Kohlstedt, H. Keppler, D. C. Rubie, Solubility of water in the α, β and γ phases of $(Mg,Fe)_2SiO_4$. *Contrib. Mineral. Petrol.* **123**, 345–357 (1996). doi:10.1007/s004100050161
3. M. M. Hirschmann, Water, melting, and the deep Earth H_2O cycle. *Annu. Rev. Earth Planet. Sci.* **34**, 629–653 (2006). doi:10.1146/annurev.earth.34.031405.125211
4. D. G. Pearson, F. E. Brenker, F. Nestola, J. McNeill, L. Nasdala, M. T. Hutchison, S. Matveev, K. Mather, G. Silversmit, S. Schmitz, B. Vekemans, L. Vincze, Hydrous mantle transition zone indicated by ringwoodite included within diamond. *Nature* **507**, 221–224 (2014). doi:10.1038/nature13080
5. S. Karato, The role of hydrogen in the electrical conductivity of the upper mantle. *Nature* **347**, 272–273 (1990). doi:10.1038/347272a0
6. T. Yoshino, G. Manthilake, T. Matsuzaki, T. Katsura, Dry mantle transition zone inferred from the conductivity of wadsleyite and ringwoodite. *Nature* **451**, 326–329 (2008). doi:10.1038/nature06427
7. L. Dai, S. Karato, Electrical conductivity of wadsleyite at high temperatures and high pressures. *Earth Planet. Sci. Lett.* **287**, 277–283 (2009). doi:10.1016/j.epsl.2009.08.012
8. A. Kuvshinov, N. Olsen, A global model of mantle conductivity derived from 5 years of CHAMP, Ørsted, and SAC-C magnetic data. *Geophys. Res. Lett.* **33**, L18301 (2006). doi:10.1029/2006gl027083
9. A. Kelbert, A. Schultz, G. Egbert, Global electromagnetic induction constraints on transition-zone water content variations. *Nature* **460**, 1003–1006 (2009). doi:10.1038/nature08257
10. A. V. Semenov, A. Kuvshinov, Global 3-D imaging of mantle conductivity based on inversion of observatory C-responses — II. Data analysis and results. *Geophys. J. Int.* **191**, 965–992 (2012). doi:10.1111/j.1365-246x.2012.05665.x
11. C. Püthe, A. Kuvshinov, A. Khan, N. Olsen, A new model of Earth's radial conductivity structure derived from over 10 yr of satellite and observatory magnetic data. *Geophys. J. Int.* **203**, 1864–1872 (2015). doi:10.1093/gji/ggv407
12. F. Civet, E. Thébault, O. Verhoeven, B. Langlais, D. Saturnino, Electrical conductivity of the Earth's mantle from the first Swarm magnetic field measurements. *Geophys. Res. Lett.* **42**, 3338–3346 (2015). doi:10.1002/2015gl063397
13. A. V. Grayver, F. D. Munch, A. V. Kuvshinov, A. Khan, T. J. Sabaka, L. Tøffner-Clausen, Joint inversion of satellite-detected tidal and magnetospheric signals constrains electrical conductivity and water content of the upper mantle and transition zone. *Geophys. Res. Lett.* **44**, 6074–6081 (2017). doi:10.1002/2017gl073446
14. T. Yoshino, T. Katsura, Electrical conductivity of mantle minerals: role of water in conductivity anomalies. *Annu. Rev. Earth Planet. Sci.* **41**, 605–628 (2013). doi:10.1146/annurev-earth-050212-124022
15. R. J. Banks, Geomagnetic variations and the electrical conductivity of the upper mantle. *Geophys. J.*

R. Astron. Soc. **17**, 457–487 (1969). doi:10.1111/j.1365-246x.1969.tb00252.x

16. U. Schmucker, Magnetic fields of external origin within the Earth (section 4.1.1.5), in *Landolt-Börnstein, Group V: Geophysics* (Springer, 1985), pp. 39–41. doi:10.1007/10201925_12
17. N. Olsen, The electrical conductivity of the mantle beneath Europe derived from C-responses from 3 to 720 hr. *Geophys. J. Int.* **133**, 298–308 (1998). doi:10.1046/j.1365-246x.1998.00503.x
18. N. Olsen, Long-period (30 days–1 year) electromagnetic sounding and the electrical conductivity of the lower mantle beneath Europe. *Geophys. J. Int.* **138**, 179–187 (1999). doi:10.1046/j.1365-246x.1999.00854.x
19. G. Balasis, G. D. Egbert, Empirical orthogonal function analysis of magnetic observatory data: further evidence for non-axisymmetric magnetospheric sources for satellite induction studies. *Geophys. Res. Lett.* **33**, L11311 (2006). doi:10.1029/2006gl025721
20. C. Püthe, A. Kuvshinov, N. Olsen, Handling complex source structures in global EM induction studies: from C-responses to new arrays of transfer functions. *Geophys. J. Int.* **201**, 318–328 (2015). doi:10.1093/gji/ggv021
21. T. Rikitake, *Electromagnetism and the Earth's Interior*, Developments in Solid Earth Geophysics, Vol. 2 (Elsevier, Amsterdam, 1966). doi:10.1016/B978-0-12-395756-6
22. I. A. Daglis, R. M. Thorne, W. Baumjohann, S. Orsini, The terrestrial ring current: origin, formation, and decay. *Rev. Geophys.* **37**, 407–438 (1999). doi:10.1029/1999rg900009
23. M. Nose, T. Iyemori, M. Sugiura, T. Kamei, Geomagnetic Dst index, World Data Center for Geomagnetism, Kyoto (2015). doi:10.17593/14515-74000
24. D. Bercovici, S. Karato, Whole-mantle convection and the transition-zone water filter. *Nature* **425**, 39–44 (2003). doi:10.1038/nature01918
25. J. F. Lawrence, P. M. Shearer, Imaging mantle transition zone thickness with SdS–SS finite-frequency sensitivity kernels. *Geophys. J. Int.* **174**, 143–158 (2008). doi:10.1111/j.1365-246x.2007.03673.x
26. F. D. Munch, A. V. Grayver, A. Kuvshinov, A. Khan, Stochastic inversion of geomagnetic observatory data including rigorous treatment of the ocean induction effect with implications for transition zone water content and thermal structure. *J. Geophys. Res. Solid Earth* **123**, 31–51 (2018). doi:10.1002/2017jb014691
27. J. Velímský, Electrical conductivity in the lower mantle: constraints from CHAMP satellite data by time-domain EM induction modelling. *Phys. Earth Planet. Inter.* **180**, 111–117 (2010). doi:10.1016/j.pepi.2010.02.007
28. P. Tarits, M. Mandéa, The heterogeneous electrical conductivity structure of the lower mantle. *Phys. Earth Planet. Inter.* **183**, 115–125 (2010). doi:10.1016/j.pepi.2010.08.002
29. J. J. Love, A. Chulliat, An international network of magnetic observatories. *Eos Trans. AGU* **94**, 373–374 (2013). doi:10.1002/2013eo420001
30. C. C. Finlay, C. Kloss, N. Olsen, M. D. Hammer, L. Tøffner-Clausen, A. Grayver, A. Kuvshinov, The CHAOS-7 geomagnetic field model and observed changes in the South Atlantic Anomaly. *Earth Planets Space* **72**, 156 (2020). doi:10.1186/s40623-020-01252-9
31. F. Clette, L. Lefèvre, International Sunspot Number V2.0 (SILSO Sunspot Number V2.0), World Data Center SILSO, Royal Observatory of Belgium, Brussels (2015). doi:10.24414/qnza-ac80

Acknowledgments: We thank the INTERMAGNET and WDC communities and the maintainers of the public model and index archives used here (*23, 29–31, 46–48*). **AI-use disclosure (Science policy):** AI-assisted tools were used for log summarization, bibliographic metadata checks, and language editing; full details are in SM §S12. The author verified all data processing, numerical results, references, figures, and interpretations and takes full responsibility for the work. **Funding:** This research was supported by the Basic Science Research Program through the National Research Foundation of Korea (RS-2019-NR040076) funded by the Ministry of Education (2026); by the Institute for Korea Spent Nuclear Fuel (iKSNF) and Korea Foundation of Nuclear Safety (KoFONS) grant funded by the Korea government (Nuclear Safety and Security Commission, NSSC) (RS-2021-KN066110); and by the National Research Foundation of Korea (NRF) grant funded by the Korea government (Ministry of Science and ICT, MSIT) (No. 2022R1A2C1092301). **Author contributions:** S.O. designed and performed the research and wrote the manuscript. **Competing interests:** The author declares no competing interests. **Data and materials availability:** all processing and experiment code, locked intermediate archives, and the gate ledger are deposited at Zenodo (doi:10.5281/zenodo.21184326); source data are public (*23, 29–31, 46–48*).

List of Supplementary Materials:

Supplementary Text (§S1 to §S12)

Figs. S1 to S9

Tables S1 to S6 (including Table S1a)

References (*32–49*)

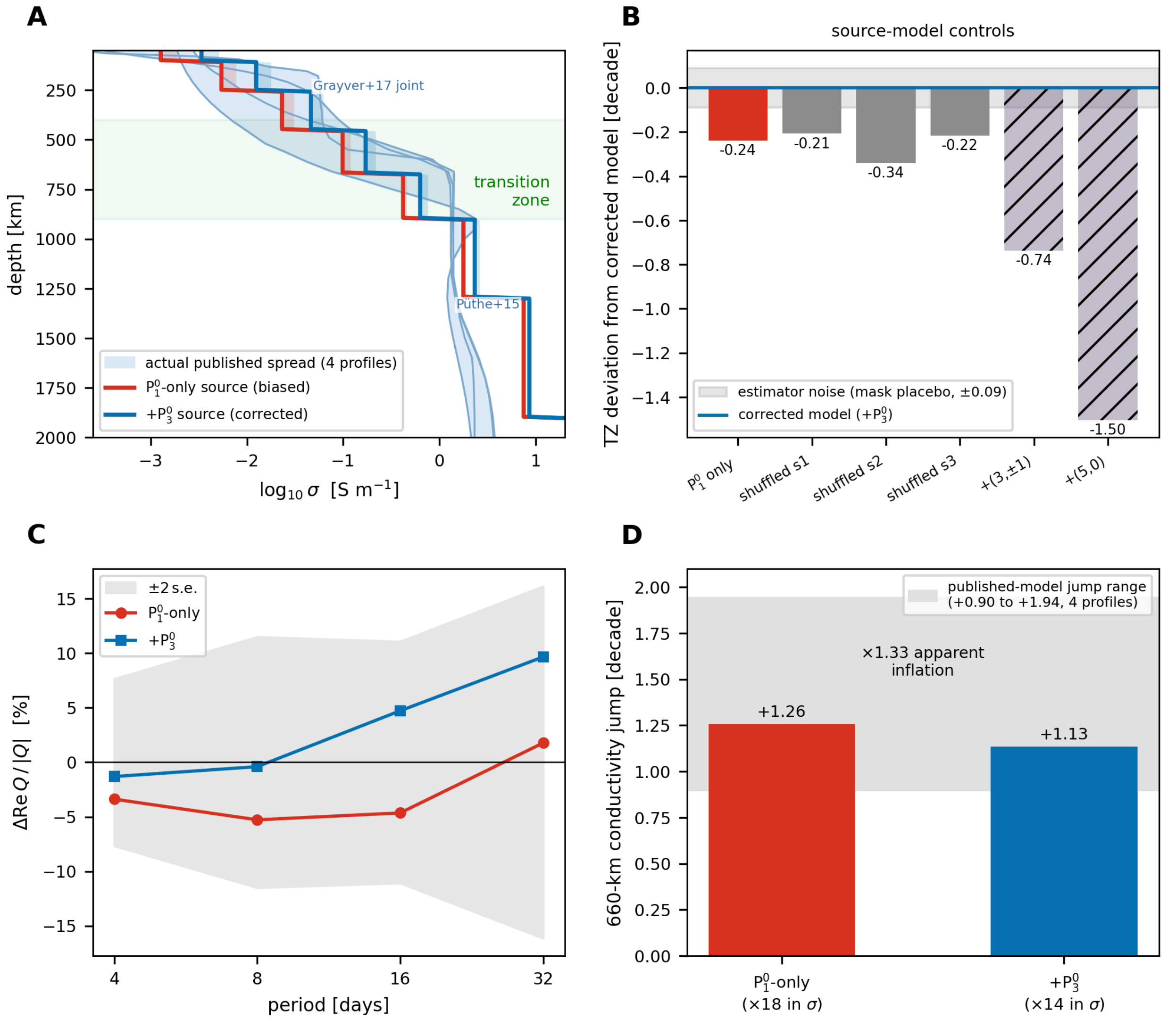

Fig. 1. Recovered conductivity and bias signatures. (A) Conductivity σ(z) for the P_1^0-only source (red)

and the +P_3^0 source (blue), over the four published profiles (Püthe+15; Grayver+17 joint, sparse, C1; shading is their 1.27-decade spread at 450–670 km). Both recovered profiles fall inside the published spread. (B) Transition-zone deviation of each control from the corrected model. Shuffled-P_3^0 geometries stay biased like P_1^0-only. The (3,±1) and (5,0) bases are not identifiable (hatched). The grey band is the ±0.09 estimator-noise floor. (C) Real part of the transfer function relative to |Q|, by period. The P_1^0-only chain suppresses it by 3 to 5 per cent; the +P_3^0 chain removes the suppression. (D) Apparent 660-km conductivity jump. The P_1^0-only source inflates it by ×1.33.

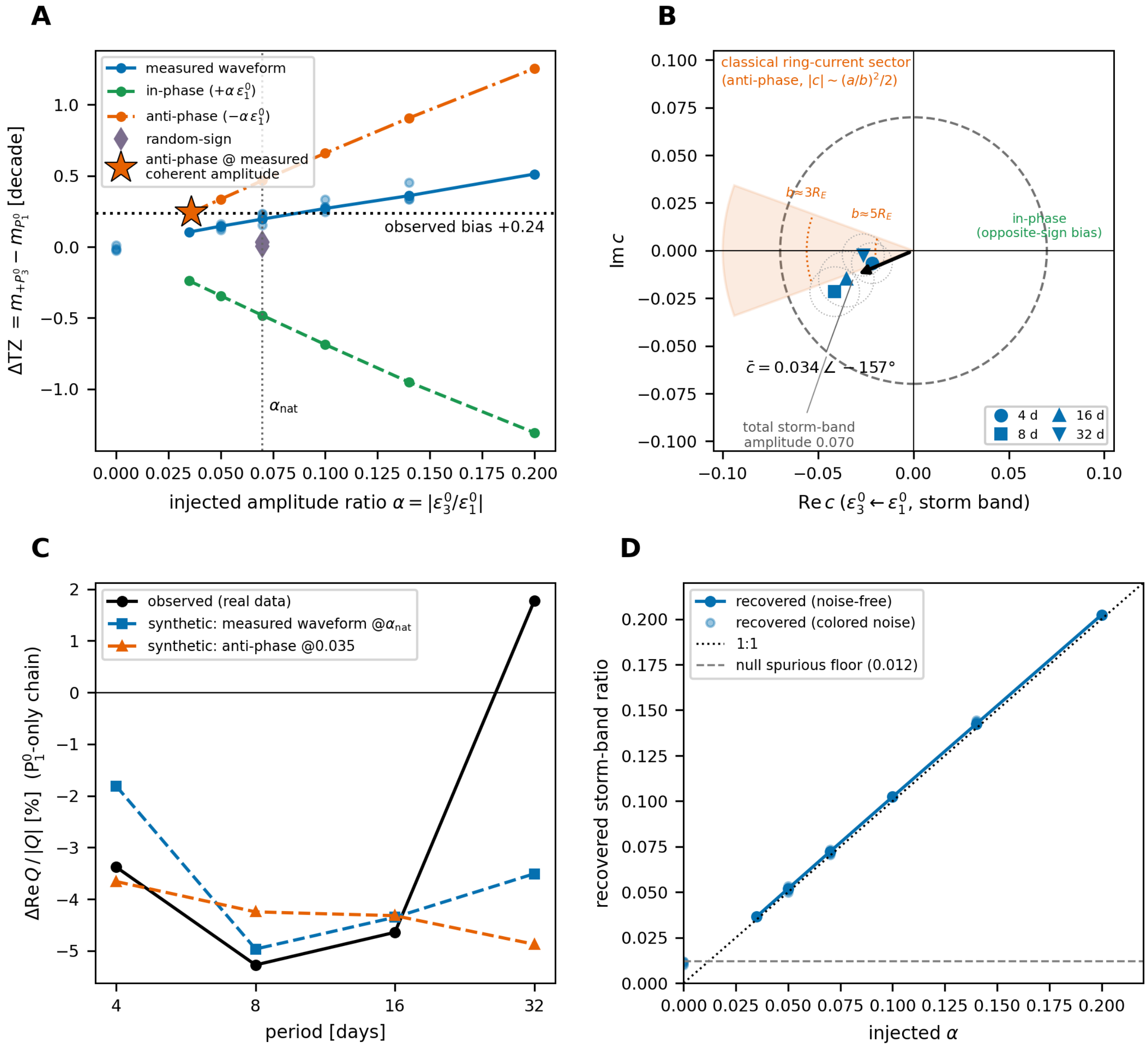

Fig. 2. Injection experiments and carrier geometry. (A) Bias transfer function ΔTZ(α) for the four injection variants: measured waveform, in-phase, anti-phase, and random-sign (Materials and Methods). The star marks the anti-phase variant at the measured coherent amplitude, which reproduces the real-data bias. (B) Storm-band carrier in the complex plane. The dashed circle is the total P_3^0 amplitude (0.070). Symbols are the Welch bins; the arrow is the variance-weighted mean $\bar{c} = 0.034\,\angle -157°$. The shaded sector marks the classical ring-current expectation. (C) Real-part signature: real data against the two synthetic injections. (D) Recovery check: recovered against injected amplitude, slope 1.

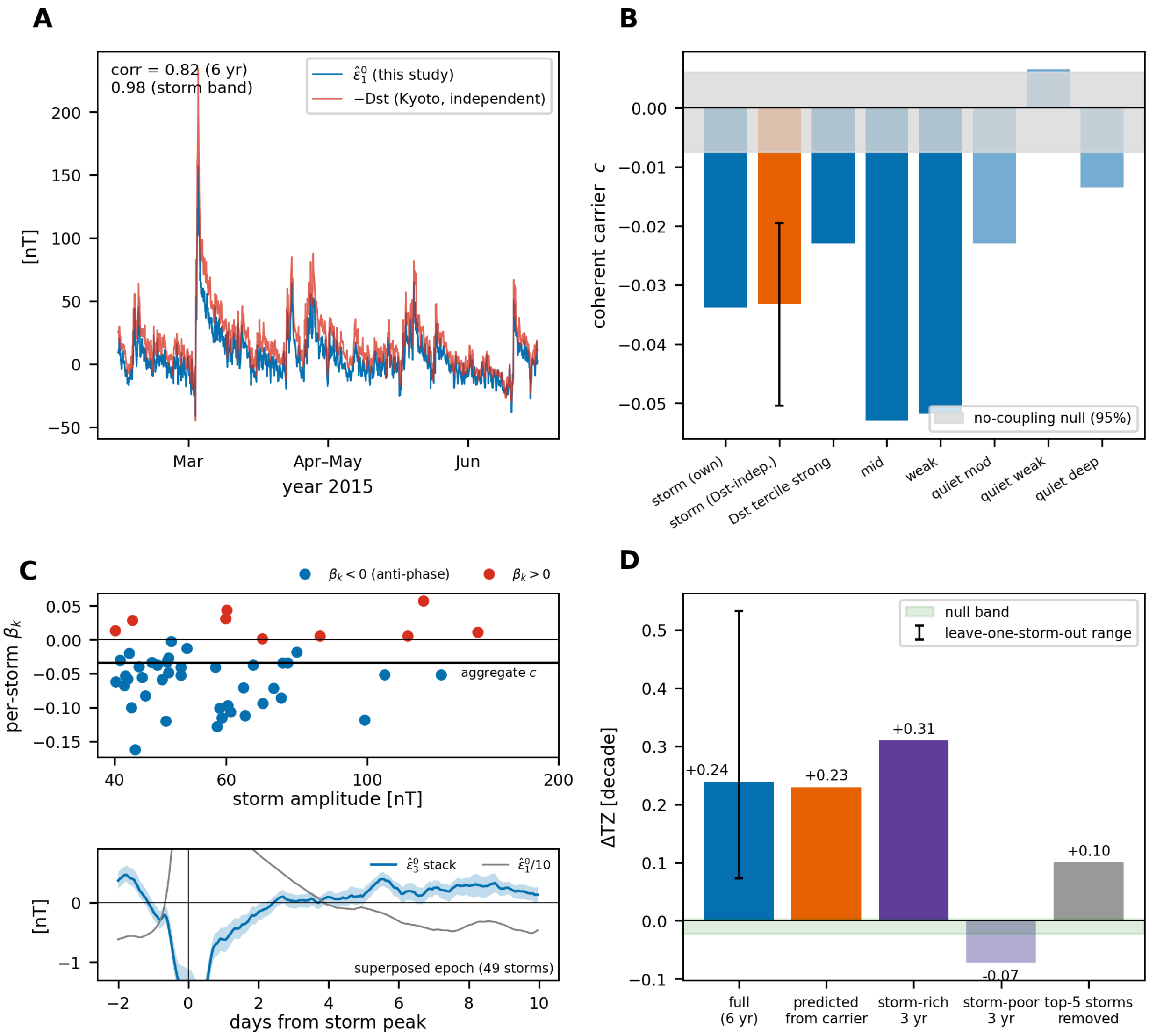

Fig. 3. Storm attribution and controls. (A) Separated main field $\hat{\varepsilon}_1^0$ against the independent Kyoto Dst index (correlation 0.82 hourly, 0.98 in the storm band). (B) Coherent carrier c by condition: own catalog, independent catalog, Dst terciles, and quiet strata, against the shift-surrogate null band. (C) Per-storm regression β_k versus storm amplitude, with the superposed-epoch stack below. (D) Paired shift for storm-rich and storm-poor years (+0.31, −0.07), the leave-one-storm-out range, and the carrier-predicted value.

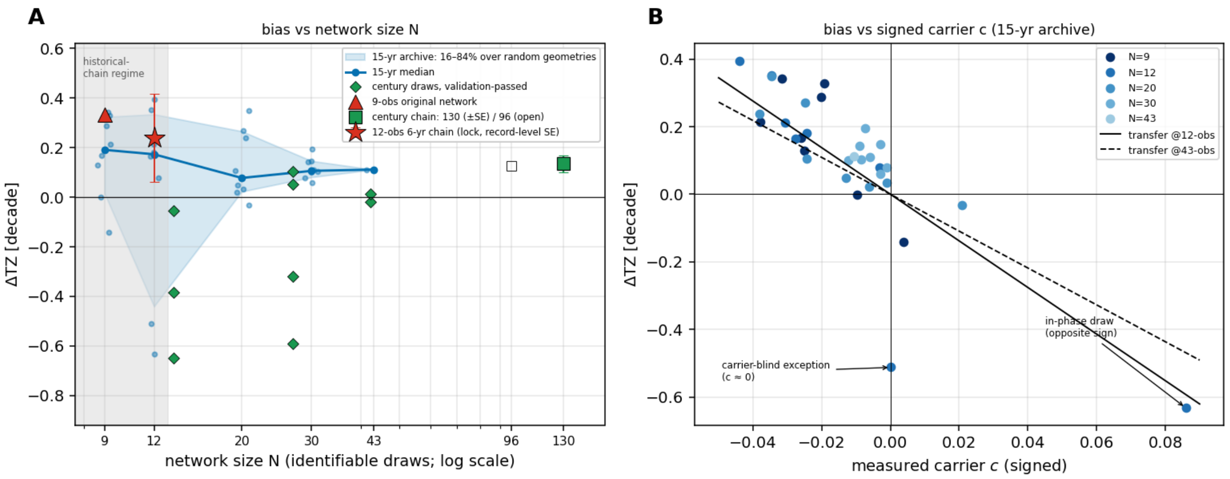

Fig. 4. Network dose-response. (A) Paired transition-zone shift against network size N. Blue: random identifiable subnetworks of the 15-year archive (median, 16–84% range, individual draws). Green: the century archive, with validation-passed random draws (diamonds) and the 96- and 130-station chains (squares). The star and triangle are the locked 12- and 9-station chains. Sparse networks scatter widely; the scatter collapses with N, and curated chains of any size stay within +0.11 to +0.24 decades. Gate-failed draws (|ΔTZ| up to 2.5–3.4 decades) are reported in SM §S11. (B) Paired shift against the signed carrier c for the 15-year draws. All draws follow the phase-selective transfer in both branches. The in-phase draw and the single carrier-blind exception (c ≈ 0, ΔTZ = −0.51) are marked.

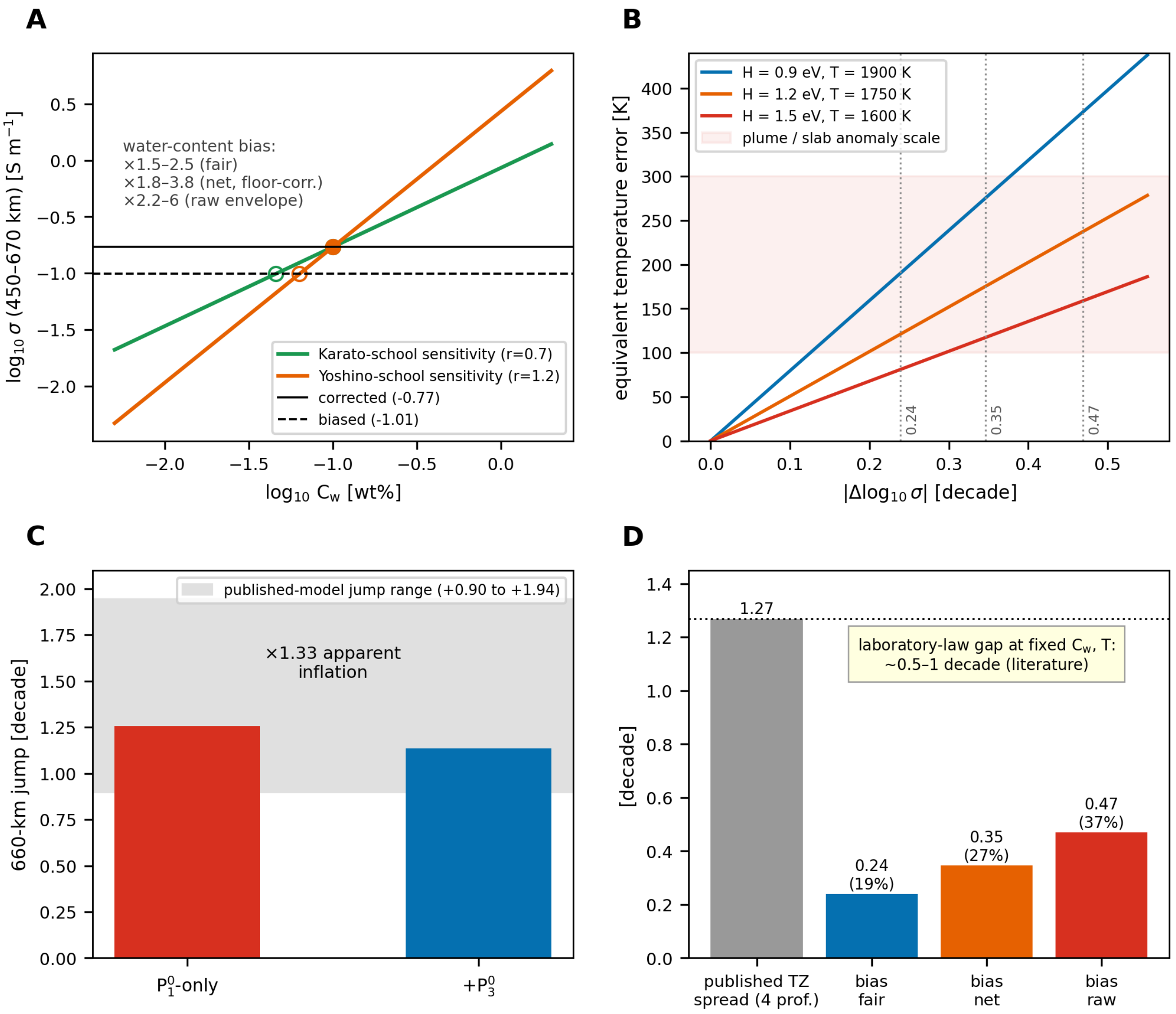

Fig. 5. Earth-consequence translation. (A) Water-content mapping under the Karato-school and Yoshino-school sensitivities. This is a diagnostic translation, not a new water measurement. The bias maps to ×1.5–2.5 in the adopted band and ×1.8–3.8 after floor correction; the raw-envelope tier (×2.2–6) is labeled. (B) Temperature equivalent (80–190 K adopted; 117–275 K floor-corrected; raw tier labeled), against the plume and slab anomaly scale. (C) Apparent 660-km jump for the two source models, against the published-model range (+0.90 to +1.94). Both fall inside it. The biased chain overstates the sharpness of the 660-km barrier. (D) Bias against the flagship inter-model spread (19–27% for the fair and floor-corrected values; the raw-envelope bar is 37%; SM §S2a).

Supplementary Materials for “A hidden component of magnetic storms makes Earth’s mantle transition zone look drier than it is”

Seokhoon Oh

Correspondence to: gimul@kangwon.ac.kr

This PDF includes: Materials and Methods (§S1–S3), Experiment designs and results (§S4–S8), Consequence translation (§S9), Pre-registered gate ledger and its revisions (§S10), Independent 15-year replication and the network dose-response (§S11), AI-use disclosure (§S12), Figs. S1 to S9, Tables S1 to S6, References (32–50).

§S1. Data and processing chain

Observatories and pre-processing. We use hourly means from 12 mid-latitude INTERMAGNET observatories (Table S4; absolute geomagnetic latitudes 22°–52°), 2014–2019 (52,584 hours), computed from definitive one-minute data (≥45 valid minutes per hour; overall availability 96.8%; the largest outage, SJG during Hurricane Maria in 2017, is retained as a realistic gap). The CHAOS-7 core field (*30*), evaluated with chaosmagpy (*38*) on a monthly grid and interpolated, is subtracted; remaining static crustal biases are absorbed by per-station median removal in the separation step. Quality control removes |residual| > 4000 nT outliers and >500 nT/h spikes. Horizontal components are rotated to centered-dipole coordinates (epoch-2015 pole).

Epoch-wise source separation. At every hour t we fit external/internal coefficient pairs $\{\varepsilon_l^m(t), \iota_l^m(t)\}$ for a basis of spherical-harmonic terms by weighted least squares across the network, with no time-domain processing. For a Schmidt quasi-normalized term $S = P_l^m(\cos\theta)\,\mathrm{trig}(m\phi)$ the observation equations are

$$X = (\varepsilon + \iota)\,\partial_\theta S, \qquad Y = -(\varepsilon + \iota)\,(\sin\theta)^{-1}\,\partial_\phi S, \qquad Z = (l\varepsilon - (l+1)\iota)S,$$

evaluated in dipole coordinates. Missing data are handled natively (an epoch is solved when ≥7 stations report); per-station medians over each station’s valid epochs are removed before the fit. The corrected source basis is {(1,0), (1,1)c, (1,1)s, (3,0)} — eight coefficients from 24 equations (X and Z rows; condition number 35.6). The biased reference configuration omits (3,0). The (1,0) pair (ε_1^0, ι_1^0) is the induction channel used downstream in both configurations.

Transfer-function estimation. The complex ratio $\hat{Q}(T) = \hat{\iota}_1^0/\hat{\varepsilon}_1^0$ is estimated with a robust segment method designed for red spectra: first-difference prewhitening (the identical filter cancels exactly in the ratio), single-line discrete Fourier coefficients (line k = 8 per segment of length 8T, 50% overlap, Hann taper) (*36*), iteratively reweighted Huber segment averaging, and leave-one-segment-out jackknife standard errors. Segments containing gaps longer than 6 h are discarded. Bins with T = 4–137 days (six bins) are used; shorter periods are excluded as ionospheric-daily-variation dominated, following standard practice (*15, 17*).

Forward operator (self-contained). For harmonic degree l, writing the poloidal scalar of the internal field as $b = rP$, the 1-D induction problem in a conducting spherical shell reduces to a single radial equation with a Robin boundary condition at the surface r = a that couples it to the external forcing,

$$b'(a) + (l/a)\,b(a) = -a\,\frac{2l+1}{l+1}\,\varepsilon(t), \qquad \iota(t) = \frac{l}{l+1}\,\varepsilon(t) + \frac{l}{a^2}\,b(a,t),$$

and an insulating-core closure $b(r_c) = 0$ (the core skin depth is ~2 km at the longest periods used, so a superconducting inner boundary is exact for our band). Finite-element discretization (mass-lumped P1 elements on a grid with controlled cell-size dynamic range) yields a generalized eigenproblem whose modal superposition gives the impulse response

$$q(t) = Q_\infty \, \delta(t) - \sum_j \tilde{a}_j \, e^{-t/\tau_j}, \qquad Q_\infty = \frac{l}{l+1},$$

where the *driving-point* structure (forcing and observation share the surface node) makes $\tilde{a}_j = \frac{l(2l+1)}{(l+1)\,a} \, u_j(a)^2 \geq 0$ *structurally* — the spherical counterpart of the non-negativity underlying D^+ theory (*32, 33*). Two analytic anchors calibrate the implementation: the DC sum rule $Q(0) = Q_\infty - \sum_j \tilde{a}_j/\lambda_j = [l/(l+1)]\,(r_c/a)^{2l+1}$ is reproduced to 2.8×10^{-8}, and the frequency response agrees with an independent thin-shell propagator oracle to ≤1.1×10^{-6} across T = 10^2–10^7 s, with second-order grid convergence. Because the data are hourly, generation, estimation, and inversion all use the *discrete-time* (zero-order-hold) transfer function of this kernel; the hourly ZOH–continuous gap (≤1.9% for T ≥ 4 d) therefore cancels by construction. The same machinery provides the degree-3 kernel used in the injection experiments (§S5).

Both degrees actually used in this study — degree-1 (the induction channel) and degree-3 (the P_3^0 carrier and its injection kernel) — are verified against the two analytic anchors and the independent oracle in Table S1a. The implementation reproduces the static (DC) sum rule to a few parts in 10^8–10^6, matches the thin-shell propagator oracle to ≤ 3×10^{-6} in relative transfer function across five decades of period, and is structurally non-negative (min $\tilde{a}_j = 0$) at both degrees. Grid refinement of the degree-1 kernel gives maximum oracle deviations of 1.8×10^{-5}, 4.5×10^{-6}, 1.1×10^{-6}, 2.9×10^{-7} at N = 600, 1200, 2400, 4800 nodes — a factor of ≈ 4 per doubling, confirming second-order convergence — while the oracle is itself self-converged to 9.9×10^{-10} (shell resolution M = 3000 → 6000). The production runs use N = 2400. Table S1a therefore makes the operator verifiable from this Supplement alone; a full pedagogical derivation appears in a methods companion currently under review (submitted to *Earth, Planets and Space*), but is not required to reproduce any operator used here.

Table S1a. Forward-operator verification (truth model A; 41 log-spaced periods, T = 10^2–10^7 s).

Check	degree n = 1 (induction)	degree n = 3 (P_3^0 carrier)
Static limit $Q_\infty = l/(l+1)$	0.5000	0.7500
DC sum-rule relative error	2.8×10^{-8}	1.4×10^{-6}
Oracle agreement, max $\lvert\Delta Q\rvert/\lvert Q\rvert$	1.1×10^{-6}	2.6×10^{-6}
Oracle agreement, median $\lvert\Delta Q\rvert/\lvert Q\rvert$	3.4×10^{-7}	8.1×10^{-7}
Structural non-negativity, min $\tilde{a}_j$	0	0

Inversion. $\hat{Q}(T)$ is inverted for an eight-layer $\log_{10}\sigma(z)$ profile (interfaces at 0, 100, 250, 450, 670, 900, 1300, 1900 km — deliberately misaligned with test-model boundaries) by Occam-style minimization (*34, 35*) with second-difference smoothing; the regularization weight (λ = 3000) is selected once on the corrected chain by a $\chi^2/n \approx 1$ scan and frozen for every configuration, bootstrap, and experiment in this study (sensitivity of the bias to this choice is quantified in §S2). Parametric bootstrap errors treat frequency bins as independent; inter-bin error correlation is neglected (a known limitation of segment-jackknife errors, stated here for transparency).

Chain validation. The separated $\widehat{\varepsilon}_1^0$ re-detects the five largest storms of 2014–2019 at correct absolute times, and correlates with the independent final Kyoto Dst index (*23*) at 0.82 (hourly, six years) and 0.98 (storm band, 1–20 days; Fig. 3A). C-responses agree with published-profile responses at the 8.8–10.1% median level over 4–64 days.

§S2. The lock: configurations, machine floor, and provenance (Experiment 0)

All source-model configurations are compared in a single run of the identical pipeline (Table S1): M0 (P_1^0-only, i.e. $n=1$ with $m \leq 1$), M1 (+P_3^0; the adopted configuration), M2 (+P_3^0 and (3,±1)), M3 (+P_3^0 and (5,0)), and three negative-control configurations Mbad1–3 in which the (3,0) spatial pattern is evaluated at station-permuted coordinates — preserving the degree-of-freedom count (eight coefficients) and conditioning (cond ≈ 29) while destroying the physical geometry.

Machine floor. The envelope-distance metric (median distance of the recovered $\log_{10}\sigma$ outside the three-model published envelope over 400–900 km) has a nonzero floor even for in-envelope truth: inverting *exact* synthetic responses of each anchor profile through the identical bins, errors, and λ yields floors of 0.098–0.255 (median 0.129) in the adopted band, and median 0.123 in the discovery band. The real-data P_1^0-only distance of 0.469 therefore contains a net data bias of +0.346.

Regularization and metric sensitivity. The paired transition-zone shift is robust to the frozen regularization: multi-start Occam solutions give $\Delta TZ = +0.269, +0.266, +0.240$ for $\lambda = 300, 1000, 3000$ (a 12% spread over a ten-fold λ range), and +0.245, +0.243, +0.218 for the alternative 400–900-km mean-difference metric. Transparency note: single-start L-BFGS exhibited a local-minimum artifact at intermediate λ (non-monotonic $\chi^2(\lambda)$); all sensitivity results quoted here use multi-start (flat, archived-solution, and λ-continuation initializations; minimum total objective adopted). The locked headline results are unaffected: bootstrap inversions are warm-started and the corrected-configuration solution matches the archived model vector to $<10^{-3}$.

Provenance. The locked run reproduces the archived discovery-stage inversion exactly: the historical P_1^0-only configuration (band $T \geq 2$ d, λ-scan → 3000) returns distance 0.469, χ^2/n 0.97, and a 660-km jump of +1.33, matching the archived log to all printed digits; the corrected configuration reproduces the archived model vector to $<10^{-3}$.

Pattern specificity. No shuffled-geometry control restores the envelope (distances 0.352, 0.468, 0.359 versus M0's 0.377 and M1's 0.200), although one permuted pattern correlates with the true P_3^0 pattern at $|r| = 0.69$. The improvement from the true geometry is therefore not a degrees-of-freedom or regularization effect.

Identifiability limits. Adding (3,±1) raises the separation condition number from 36 to 1284; adding (5,0) raises it to 200 and collapses the recovery (distance 1.69): with 12 mid-latitude stations and $X{\cdot}Z$ rows, zonal degrees beyond P_3^0 are not identifiable (see §S8 for the latitude-leverage analysis). This bounds the usable source basis rather than the physics.

§S2a. The actual published-model spread, and where the bias hides

The three-profile benchmark of §S2 is a *representative* set used as the discovery-era internal anchor. To compare against the literature itself we assembled verifiable published 1-D profiles: the 40-layer model of Püthe *et al.* (Table 2 of *11*, free access) and the three magnetospheric/joint profiles of Grayver *et al.* (author-published repository with citation DOI; *13, 46*). Two further candidates (the 3-D models of Kelbert *et al.* (*9, 47*) and Sun *et al.* (*39, 48*) hosted at IRIS EMC) were downloaded but excluded from quantitative use: their netCDF files resolve laterally sparse subvolumes (0–20% of transition-zone cells defined), so a global-average 1-D profile cannot be defended from those files; manual digitization of the papers' profile figures is noted as optional reinforcement.

The result reframes the comparison. The actual spread between flagship satellite-era models is **1.27 decades** at 450–670 km (1.11 over 400–900 km) — three times the representative benchmark's spread — dominated by the genuine disagreement between the resistive transition zone of (*11*) and the conductive one of (*13*). Against this envelope, *both* the biased and the corrected profiles of this study lie inside (distance 0.000): the source-geometry bias is invisible to external model comparison, exactly as it is to internal consistency metrics (§S3). The paired bias of +0.24 (fair band; +0.35 floor-corrected, +0.47 raw) amounts to **19%, 27%, and 37%** of the actual transition-zone spread, respectively — the basis for the main-text statement that a substantial fraction of the literature's disagreement could be carried by source-geometry treatment. All profiles, the coverage audit, and the recomputation are in `models_published/` with the build script.

Verification of the spread figure. The Püthe *et al.* table was extracted twice independently from the free-access article page with identical results and four spot-checked values; the Grayver *et al.* profiles were loaded mechanically from the authors' repository, and the column definitions were confirmed against the text of the authors' manuscript (C1 = inversion of magnetospheric C-responses; M2 = tidal-only, excluded here as an upper-mantle channel; joint = both). The 1.27-decade median spread was recomputed through an independent code path (1.268), and the most conservative single pair — Püthe *et al.* versus the Grayver *et al.* joint model — differs by 1.15 decades. Two caveats are carried: (i) part of the 1-D spread reflects differing sensitivity bands and regularization (the Püthe *et al.* model's sensitivity peaks at 800–1200 km, so its resistive transition zone is partly prior-dominated) rather than contradictory data — which itself illustrates how strongly chain choices shape published profiles; (ii) the spread among 1-D *models* is distinct from the ~1-order-of-magnitude *lateral* heterogeneity mapped by 3-D studies (*9*, *44*) and should not be conflated. We note in passing, from the authors' manuscript, that even this flagship 2017 chain estimates its magnetospheric responses from the (1,0) term alone — the exposure indicator this paper proposes to audit (the satellite-chain leakage structure differs from the ground-array mechanism quantified here and is not claimed to be identical; Table S6).

§S3. Internal-consistency blindness

Every internal quality metric prefers the biased configuration: misfit χ^2/n (0.25 versus 0.46), agreement with an independent broadband estimator of the same data (8.6% versus 12.6%), and distance to published *response* shapes (8.8% versus 10.1%). The reason is structural: per-epoch leakage of the anti-phase internal degree-3 response into the apparent degree-1 pair produces a *smooth, internally consistent, 1-D-representable* — but wrong — transfer function. A wrong Earth fitted to a wrongly separated source remains self-consistent. Only external anchors (the published-model envelope calibrated by the machine floor, and independent activity indices) detect the bias. We regard this as the central operational lesson of the study.

§S4. Null synthetic: the extra term is harmless when nothing is there (Experiment 1)

Design. Truth Earth: a five-layer test profile. Truth source: degree-1 only ($m \leq 1$), using the *real* separated coefficient time series as source waveforms (preserving true storm timing, spectra, and activity), with internal responses generated by the truth kernel; observations are synthesized at the real station coordinates with the real availability mask. Noise: (v1c, primary) the real M1-fit residuals re-injected by 2192-h block bootstrap — preserving amplitude, coloredness, and inter-station correlation while destroying alignment with the source; (v1) iid Gaussian matched to per-station residual standard deviations; (v0) 0.3 nT white. Twelve paired realizations per noise family: each noise realization is processed twice, with and without the (3,0) term, so differences isolate the extra degree of freedom.

Results. Under realistic colored noise the extra term moves the transition-zone layer by $\Delta TZ = -0.014$ (median; range −0.023 to +0.002) — the real-data effect (+0.239) lies outside all twelve null realizations, with opposite sign. Both configurations recover the truth at the oracle floor (log-RMS 0.184/0.187 versus floor 0.179). The spurious P_3^0 amplitude manufactured by the chain from noise alone is 0.012 (storm-window ratio), against 0.070 measured in the real data (×5.8). An iid noise model overstates the null variance by ×19 — the basis for a documented gate revision (§S10). Machinery sanity: noise-free truth-direct estimation errs by 0.47% (median); noise-free separation recovers the source waveform with correlation 0.999998.

§S5. Injection experiments: the bias transfer function and its phase selectivity (Experiment 2)

Design. To the §S4 truth we add a controlled P_3^0 source with internal response from the degree-3 truth kernel ($Q_3 < Q_1$; e.g. at $T = 16$ d, $Q_1 = 0.320+0.052i$ versus $Q_3 = 0.255+0.100i$ — the contrast that powers the bias). Injection amplitude is calibrated by the storm-window ratio $\alpha = |\varepsilon_3^0/\varepsilon_1^0|$ (moving-average band 1–20 days). Waveform variants: **A**, the real measured $\hat{\varepsilon}_3^0$ waveform rescaled ($\alpha = \alpha_{\text{nat}} = 0.0699$ is the real operating point); **B**, $+\alpha\cdot\varepsilon_1^0$ (in-phase coherent limit); **B**$^-$, $-\alpha\cdot\varepsilon_1^0$ (anti-phase limit); **C**, storm-windowed with random per-storm sign (globally incoherent).

Coherence of the real waveform. Band-wise regression of $\hat{\varepsilon}_3^0$ on $\hat{\varepsilon}_1^0$ gives $|c| = 0.023, 0.047, 0.038$ ($\pm$~0.013) at 4, 8, 16 days with phases −163°, −153°, −157° — a consistent anti-phase coherent component of mean amplitude $\alpha_{\text{coh}} = 0.0359 \pm 21\%$, i.e. about half the total amplitude. The variance-weighted complex mean is $\bar{c} = 0.0337\,\angle{-156.9^\circ}$ with a combined phase uncertainty of ±12.2°: the deviation from pure anti-phase (+23.1°) is 1.9σ — not significant, with local-time structure of the storm-time current system as the candidate explanation should longer records resolve it. Estimator consistency: $|\bar{c}| = 0.0337$ (spectral, weighted) versus $c_{\text{storm}} = -0.0338$ (time-domain projection, §S6) — the two routes agree to 0.3%.

Results (Table in Fig. 2A; noise-free unless stated). The transfer function is linear in the coherent amplitude and sign-selected by phase: $\Delta TZ \approx +2.88\alpha - 1.7\alpha^2$ for the measured waveform; $-7.14\alpha + 2.9\alpha^2$ for in-phase; $+6.89\alpha - 3.0\alpha^2$ for anti-phase; ≈ 0 ($\leq +0.04$ at $\alpha = 0.07$) for random-sign. Closure: injecting the measured waveform at its native amplitude reproduces +0.195 (×0.82 of the observed +0.239; colored-noise ensemble median +0.215, ×0.90), and the anti-phase limit evaluated at the measured coherent amplitude gives +0.241 (×1.01; to be read within the ±21% uncertainty of α_{coh}). The synthetic short-period Re-suppression signature matches the observed one (Fig. 2C). Recovery check: the corrected configuration recovers injected waveforms with correlation ≥0.999 and 1:1 amplitude across the sweep (Fig. 2D). The geometric pathway is quantified by projecting the (3,0) patterns onto the degree-1 basis at the network: the internal-degree-3 pattern projects onto the apparent external-degree-1 channel with coefficient +0.97 (and onto the apparent internal channel with −0.25), so an anti-phase internal n=3 field weakens the apparent response — a less conductive mantle.

Residual budget. The ~18% shortfall of variant A against the observed shift bounds, *within this diagnostic*, contributions from Earth-model differences (the synthetic truth's Q_3/Q_1 contrast versus the real Earth's) and any non-P_3^0 structure that the (3,0) term absorbs in the real data (3-D and ocean effects, residual ionospheric leakage).

§S6. Storm attribution, recurrence, and the estimator-noise floor (Experiment 3)

Carrier machinery. Storm-band series are formed as $\text{bp}(x) = \text{MA}_{24}(x) - \text{MA}_{480}(x)$ (zeros at daily harmonics; passband ≈1–20 days). For each of the 49 self-detected storms (peak threshold 40 nT, ≥5-day separation), windows [−24 h, +120 h] around the peak define per-storm projections $\beta_k = \langle e_3 e_1\rangle_k / \langle e_1^2\rangle_k$ and the energy-weighted aggregate $c_{\text{storm}} = \sum S_{xy} / \sum S_{xx} = -0.0338$ (storm-bootstrap 95% CI [−0.052, −0.017]). Sign consistency: 75% of the 24 highest-energy storms (82% of all) have $\beta_k < 0$.

Null models. (i) *Zero-coupling surrogate*: circularly shifting $\hat{\varepsilon}_3^0$ by a random lag (preserving both autocorrelations and seasonality, destroying the cross-coupling) gives a 95% band of [−0.0075, +0.0060]; none of 300 surrogates reaches the measured |c| (empirical $p < 1/300$). (ii) *Random calendar placebo*: 49 random non-storm windows give mean −0.020 — placebo windows also couple, because sub-threshold recurrent activity carries the same-signed relationship; quiet epochs overall give $c_{\text{quiet}} = -0.0118$ (×1/2.9 of storm windows). The correct reading is a *continuous* source-geometry relationship enhanced ×2.9 in storms — the basis for a documented null-model revision (§S10).

Phase structure. Main-phase and recovery-phase projections are both anti-phase (−0.037, −0.043). A superposed-epoch stack of $\text{bp}(\hat{\varepsilon}_3^0)$ across the 49 storms shows the anti-phase waveform directly (Fig. 3C).

Recurrence versus episodic energy. The five highest-energy storms contribute only 9% of the coherent cross-power; removing them *strengthens* the aggregate (−0.0488), and every leave-one-storm-out estimate stays within 17% of the full value. The carrier is recurrent. The *energy* of the inversion-level bias is, however, episodic: splitting the record into storm-rich (2015–2017, 82% of storm energy) and storm-poor (2014, 2018, 2019) year-blocks (common band T = 4–32 d) gives ΔTZ = +0.310 versus −0.072, the latter consistent with zero at the estimator noise.

Estimator-noise floor. Masking experiments quantify the noise of inversion-level re-sampling: leave-one-storm-out ΔTZ values scatter with $\sigma = 0.098$, while masking a single random *quiet* window of the same length scatters $\sigma = 0.090$ (ratio ×1.1) — i.e. single-event ΔTZ attribution is at the noise floor of segment recomposition at this record length; the carrier c (17% jackknife variation) is the precise instrument. Five-window placebo masking ($\sigma = 0.091$) likewise explains the non-monotonic top-N removal sequence.

Prediction closure. Feeding $|c_{\text{storm}}| = 0.0338$ through the B^- transfer function of §S5 predicts ΔTZ = +0.230, against +0.239 measured (×0.96) — closing the causal chain source-measurement → transfer → conductivity error with two independent routes (×0.96 time-domain; ×1.01 spectral).

§S7. External channels: independent indices and the quiet residue (Experiment 6)

Independent storm selection. Final Kyoto Dst (*23*), fetched monthly for 2014–2019 (100% complete), correlates with our separated $\hat{\varepsilon}_1^0$ at 0.818 (raw hourly) and 0.979 (storm band). Selecting storms *from Dst alone* (min Dst < −50 nT, ≥5-day separation) yields 73 events whose windows overlap our self-detected windows by only 66%, yet the carrier reproduces at c = −0.0333 [−0.051, −0.020] — ×0.99 of the self-catalog value. Any circularity from self-selected storms is thereby excluded.

Intensity stratification. Splitting our storms by independent intensity (min Dst terciles at −98/−72 nT) gives c = −0.023 (strongest), −0.053, −0.052: the *ratio* is weakest in the very largest storms — consistent with the top-5-energy result of §S6 and with dilution of the axisymmetric anti-phase geometry by strongly asymmetric (partial) ring currents in extreme events. A per-storm Spearman test against our asymmetry index gives $\rho = -0.22$ ($p = 0.12$) — a non-significant hint in the *opposite* direction; the question is flagged open pending longer records (§S10 watch items).

The quiet residue is not the carrier. Stratifying quiet epochs by Dst (deep: > −5 nT; weak ring: −20 to −5; moderate: −40 to −20) gives c = −0.0134 [−0.026, −0.000], +0.0066 [n.s.], −0.0230 [−0.038, −0.010]: *not* monotonic in ring-current intensity. The continuous-ring-current explanation for the small quiet-time coherent residue is therefore rejected; an ionospheric (Sq/annual) leak into the (3,0) channel is the leading candidate (monthly rms modulation 32%). Equinox/solstice splits (−0.010/−0.013) cannot discriminate because ring-current activity itself peaks at equinoxes (*37*). This residue does not carry the bias — the storm-band component does (§S5–S6) — and the main text accordingly attributes the bias to the *storm-time* anti-phase component only.

The carrier survives gold-standard Sq removal. To confirm directly that the storm-band carrier is not a daily-variation artefact, we re-ran the separation after subtracting, per station, a sun-synchronous quiet-day Sq model — the local-time (UT-hour × month) median built from the quietest 40% of hours, the standard pre-processing of ASY/Dst derivation, which removes the daily variation while preserving the episodic storm-time partial ring. This removes real, local-time-organized Sq power that a global low-degree fit cannot: the broadband (3,0) diurnal-Sq fraction drops from 35% to 12%. Yet the storm-band carrier is unchanged ($|c| = 0.033 \rightarrow 0.033$; phase −165° → −166° at 4–16 d) and the degree-1 channel is preserved (correlation 0.98). The daily-variation contamination sits at periods of a day and shorter, separated from the multi-day band ($\geq$ 2 d) that the carrier and the inversion occupy; the carrier — and therefore the bias it drives — are robust to the choice of Sq treatment.

The carrier survives removal of the storm-time local-time anomaly. The quiet-day subtraction above removes only the quiet ionospheric climatology; storm-time ionospheric currents (the disturbance daily variation and DP2-type dayside enhancements) are also local-time-organized but are conditioned on disturbance, so a separate test is required. We build, per station, the storm-window local-time template — the median field in each of 24 local-time bins over all storm windows (peak −24 to +120 h) — subtract its local-time-varying component (median amplitude 6.2 nT in X; a real, removable LT-fixed storm-time disturbance) within the storm windows, and re-run the full separation. The storm-band carrier is unchanged ($|c| = 0.033 \rightarrow 0.032$; phase −165° → −165°) and the degree-1 channel is preserved (correlation 0.999). A local-time-locked storm-time source carrying the carrier would be captured by this template and removed with it; a UT-global zonal magnetospheric source is not, because storm timing is random in local time. The carrier therefore behaves as a UT-global storm-time magnetospheric signal, not a dayside or local-time-organized ionospheric one. (A naive dayside/nightside subnetwork split is not a valid form of this test: the instantaneous night hemisphere is a longitude-half subnetwork, which fails the zonal-degree identifiability requirement of §S8.)

Separately, the Gauss separation resolves each harmonic into external and internal parts from their distinct X/Z signatures, so the (3,0) carrier is the *external* coefficient alone: from our own transfer function the induced share $|Q|/|1+Q|$ is ≈ 20–25% across the storm band (2–64 d), and the carrier carries none of it — unlike a same-harmonic ground-based index, which conflates that fraction — so the carrier cannot be an induction artefact of the storm field.

Auroral channel. Hourly AE could not be retrieved programmatically (the WDC monthly pages are plot-only; the index requires the manual request service); the AE-discrimination test is deferred and marked SKIP in the gate ledger. Exposure to auroral contamination is bounded by the mid-latitude station selection ($\leq$52°) and the Dst-locked attribution above.

§S8. Network robustness and identifiability (Experiment 4)

Station jackknife. Removing any one of the 12 stations leaves the carrier negative in 12/12 cases with $\leq$35% variation. Inversion-level ΔTZ scatters with $\sigma = 0.18$ under station removal (the separation operator itself changes) — consistent with one of twelve values falling marginally below zero by chance, which is what is observed (−0.013 when removing NGK). Carrier-predicted bias tracks the jackknife ordering (correlation +0.65) while the amplitude scatter is noise-dominated (~6× the prediction-band width). NGK is also the station with the largest local-field residual (Z-ratio 2.87); since the carrier is unchanged without it (−0.0367) and the worst-two-removed network retains the effect, we classify this as estimator noise but flag it as a watch item for longer records.

Structured subsets. An inland-only network (7 stations; coastal HON, SJG, GUI, HER, EYR removed) retains the carrier and the bias ($c = -0.0365$, $\Delta TZ = +0.185$), excluding an ocean-induction artifact. Longitude halves (cond 40/58) preserve the carrier sign (−0.029/−0.054). Latitude halves do not separate at all (cond

313 low-half with sign flip, 1207 high-half): **the identifiability resource for zonal-degree separation is latitude span, not station count** — a network-design rule that also explains the §S2 order limits and guides sparse-era archive work.

§S9. Consequence translation

Laboratory conductivity laws disagree in absolute calibration by ~0.5–1 decade at fixed water content and temperature (*14*); we therefore translate the bias through *sensitivity* parameters only, in which prefactors cancel. Water: $\Delta \log_{10} C_w = \Delta \log_{10} \sigma / r$ with r ∈ [0.6, 1.4] bracketing both laboratory schools (*6, 7, 14*). Temperature: $\Delta T = \Delta \log_{10} \sigma \cdot \ln 10 \cdot k_B T^2 / H$ with H ∈ [0.9, 1.5] eV and T ∈ [1600, 1900] K. Results in Table S5. The 660-km contrast translation uses the locked inversion vectors; the inter-model-spread and jump-range comparisons use the verifiable published profiles of §S2a.

Dry-floor correction (v2). An interpreter inverts measured conductivity for water content through $\sigma_{\text{total}}(C_w, T) = \sigma_{\text{dry}}(T) + A\, C_w^r$. For a bias $\sigma_{\text{biased}} = \sigma_{\text{true}} \cdot 10^{-\Delta}$, the water-content bias factor is

$$F = C_w^{\text{true}} / C_w^{\text{biased}} = \left[\frac{1 - \rho}{10^{-\Delta} - \rho} \right]^{1/r}, \qquad \rho \equiv \sigma_{\text{dry}} / \sigma_{\text{true}},$$

which reduces to the pure-exponent result $10^{\Delta/r}$ as $\rho \to 0$ and *grows* with ρ: contrary to the intuition that a dry floor "buffers" the inference, inversion divides by the floor-suppressed sensitivity, so the floor amplifies the bias. For $\rho \geq 10^{-\Delta}$ the biased conductivity falls below the dry floor and no water solution exists — the verdict flips to "dry" (thresholds ρ ≥ 0.58, 0.45, 0.34 for Δ = 0.239, 0.346, 0.469). Numerically (fig. S8): in the Karato-school dry-value regime (ρ ≈ 0.01–0.10 at the corrected transition-zone conductivity of 0.17 S m^{-1}) the v1 factors hold, F ≈ ×1.6–2.5 (fair band); in the Yoshino-school regime (ρ ≈ 0.2–0.6) F ≈ ×1.9 upward, and the discovery-band bias crosses the dry-flip threshold — a wet transition zone misread as dry. The v1 sensitivity-only factors quoted in the main text are therefore lower bounds. We emphasize that this analysis does not re-adjudicate the laboratory debate (*6, 7, 14*); it shows that the data-side systematic and the laboratory uncertainty compound multiplicatively, and that resolving the transition-zone water question requires closing both. Caveats: the transfer-function slope of §S5 inherits the synthetic truth's Q_3/Q_1 contrast (tens of percent); temperature equivalents assume a single thermally activated mechanism, which the (H, T) bracket absorbs; absolute curves in Fig. 5A are anchored at the measured corrected conductivity and are illustrative only.

§S10. Pre-registered gates and their documented revisions

Every experiment ran against gates written before execution. Six gates were revised after first execution; each revision is recorded with its reason in the working ledger and summarized in Table S2. We emphasize what the revisions are and are not: in five of six cases the *criterion question* was corrected (a null model replaced by the appropriate one, a baseline referenced correctly) and the revised gate was then re-validated against *newly added* controls (shift surrogates, mask placebos) rather than re-judged on the same evidence; only one revision (E1a) loosened a numeric threshold, on the measured representation limit of the longest-period bin. No gate was revised by moving a threshold toward a desired outcome. The recurring lesson, learned three times independently and then fixed as policy: *at this record length, inversion-level re-sampling (window masking, storm removal, station deletion) carries σ ≈ 0.1–0.2 decades of estimator noise; the precise instrument for sensitivity tests is the carrier c, and ΔTZ may only be gated against its measured noise floor.*

Revisions: (1) E1a welch tolerance 2%→2.5% (longest-bin representation limit); (2) E1b "tie under iid noise" → "real effect outside the colored-noise null" (iid noise overstates null variance ×19; a noise-*model*-

dependent quantity must not be gated); (3) E2d immunity referenced to the $\alpha = 0$ colored-noise baseline rather than the noise-free reference (common-mode baseline −0.043); (4) E3b null changed from random-calendar placebo to circular-shift surrogate (the placebo asks storm-*exclusivity*, the wrong question for a continuous source; the surrogate asks coupling-*reality*); (5) E3v single-threshold verdict replaced by a two-level carrier/energy verdict with mask-placebo controls; (6) E4a strict ΔTZ positivity replaced by carrier-primary criteria plus noise-consistent ΔTZ bounds (expected ~1 of 12 sub-zero values under the measured σ). Watch items carried forward: the NGK coincidence (§S8); the strong-storm ratio-dilution direction (§S7); the quiet-residue identity (§S7).

§S11. Independent 15-year replication and the network dose-response

Archive. 57 observatories, 2010–2024 (CHAOS-7 valid-range cut; 43 retained by a ≥90%-availability continuity filter), processed by the identical frozen pipeline. Chain validation: the separated ring-current series correlates with the final Kyoto Dst at +0.90 over 2012–2019 (degraded to ~+0.4 in 2010–2011, a known baseline-wander era, and in 2020–2024, unattributed — both flagged and era-gated where relevant).

Replication. The paired bias replicates in sign (+0.11 full span; +0.14 era-gated), the carrier is negative and outside its no-coupling null (−0.011 [−0.019, −0.003]), and a Dst-selected catalog (188 events, 2010–2024) reproduces it at ×1.4. Geometry-leakage and injection-calibrated transfer both scale down together from the 12-station to the 43-station network (+0.97→+0.78 and 6.9→5.5 per unit carrier; ratio 0.81 ≈ 0.79), confirming the mechanism on the new network.

Dose-response. A 2×2 attribution grid (network × period) shows the amplitude change is carried by the *network*, not the period: over matched 2014–2019 epochs, 9-, 12-, and 43-station networks give ΔTZ = +0.33, +0.24, +0.11 and carriers −0.040, −0.034, −0.007. Random identifiable subnetworks (latitude span ≥25°, condition ≤150) show the full structure (Fig. 4): sparse draws are a geometry lottery (12-station 16–84% width ≈0.8 decades, including sign flips), collapsing to ±0.03 by 30 stations; the draws align along the phase-selective transfer in both branches — an in-phase draw ($c = +0.086$) produces the predicted opposite-sign bias ($-0.63 \approx -7c$). One sparse geometry is carrier-blind ($c \approx 0$ yet ΔTZ = −0.51, multi-start-confirmed): the storm-band carrier is a necessary but not sufficient exposure diagnostic at pathological sparse geometries, and the dense-network limit is the safe regime. The 43-station closure (×0.52) likewise indicates a non-coherent residual pathway that grows in relative weight as the coherent carrier shrinks — both are carried as limitations.

Century-scale archive (third record). The century points in Fig. 4 come from applying the same P_3^0 audit to a 130-observatory hourly chain assembled from the World Data Centre archive, era-gated to 1940–2020 and validated by pre-registered gates; the chain code and the locked layer-shift archives are included in this paper's deposit. The full conductivity *sounding* of this century archive is beyond the scope of the present study; every century value used here regenerates deterministically from the chain code and locked archives in this paper's deposit (§S11). The paired A/B isolates the same quantity as our shorter records — the transition-zone (450–670 km) layer shift between a P_1^0-only and a P_1^0+P_3^0 epoch-wise separation, on the same eight-layer inversion grid — with one sign-convention difference (the locked layer archives store WITHOUT−WITH; we negate on import, verified by an assertion in the figure script). Headline values (our convention): **+0.135 ± 0.034 decades at 130 stations (4σ)**, +0.126 at a 96-station subset, with the chain misfit *improving* when the term is added (χ^2/n 1.41 → 1.07). Its 20-draw random-subnetwork envelope carries pre-registered chain-validation gates (anchor deviation ≤25% AND reduced misfit in [0.3, 3]): at twelve stations only 3/8 draws pass (38%), and validated draws span −0.65 to −0.06 decades in this pool — sign skew opposite to the 15-year pool, underscoring that the sparse-regime sign is set by the draw's geometry, not universally; gate-failed draws reach |ΔTZ| = 2.5–3.4 decades and are all caught by the gates. Two synthetic controls through the same machinery close the loop: a negative control (no (3,0) term in the world) returns |ΔTZ| ≤ 0.002 under both geometries — excluding analysis false positives — and a positive control reproduces decade-scale shifts whose *sign follows the injected component's phase relation to the ring current*, the same phase selectivity isolated in §S5. The three-record concordance quoted in the main text (6-year +0.24 ± 0.18; 15-year +0.11 ± 0.07; century +0.135 ± 0.034; records differing in data source, station set, era, and internal-field treatment) uses that study's record-level standard errors.

Figs. S1–S9

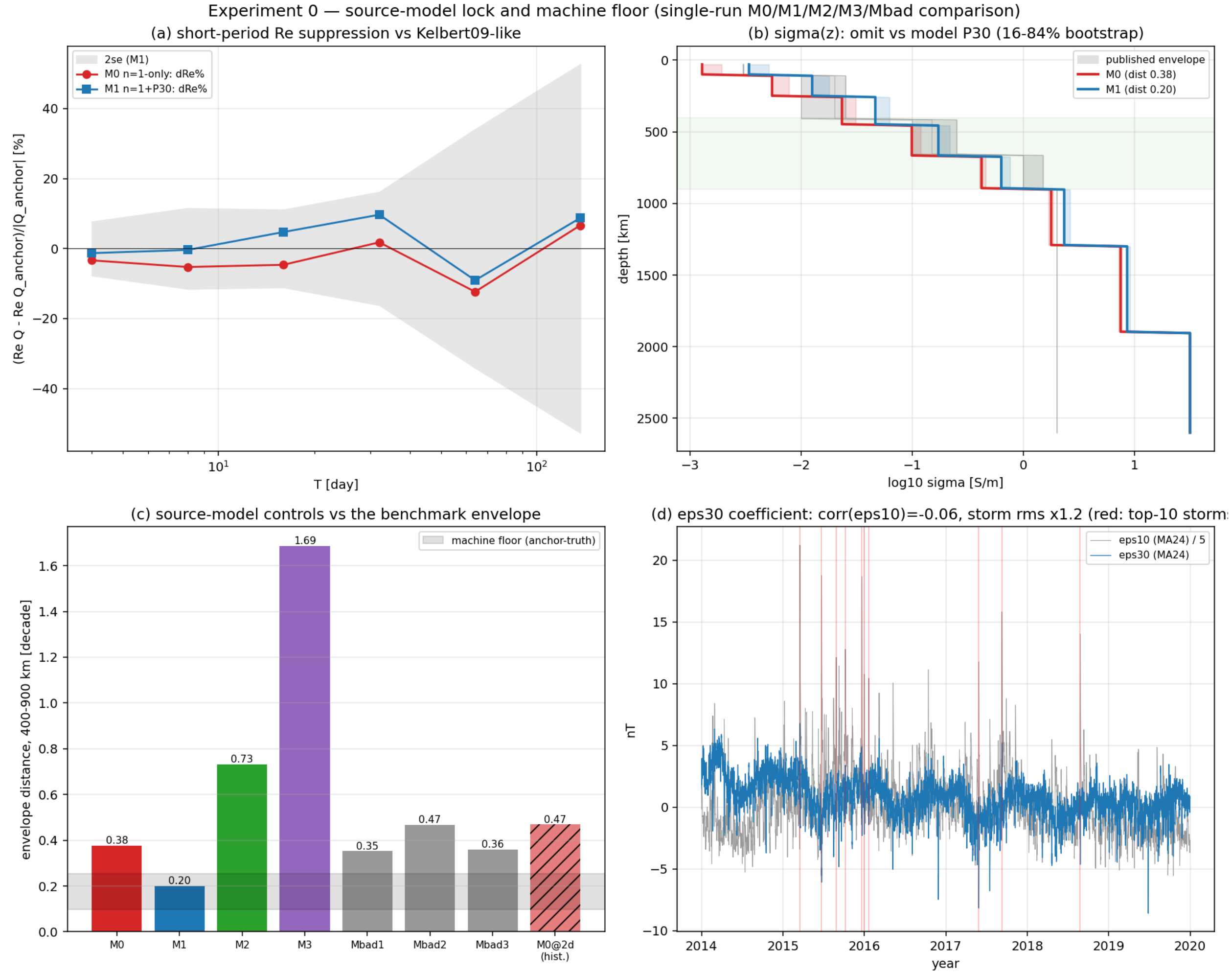

Fig. S1. single-run lock of all source-model configurations; bin tables; ε_3^0 quick-look.

Experiment 1 — null synthetic on an n=1-only truth (operating-point matched)

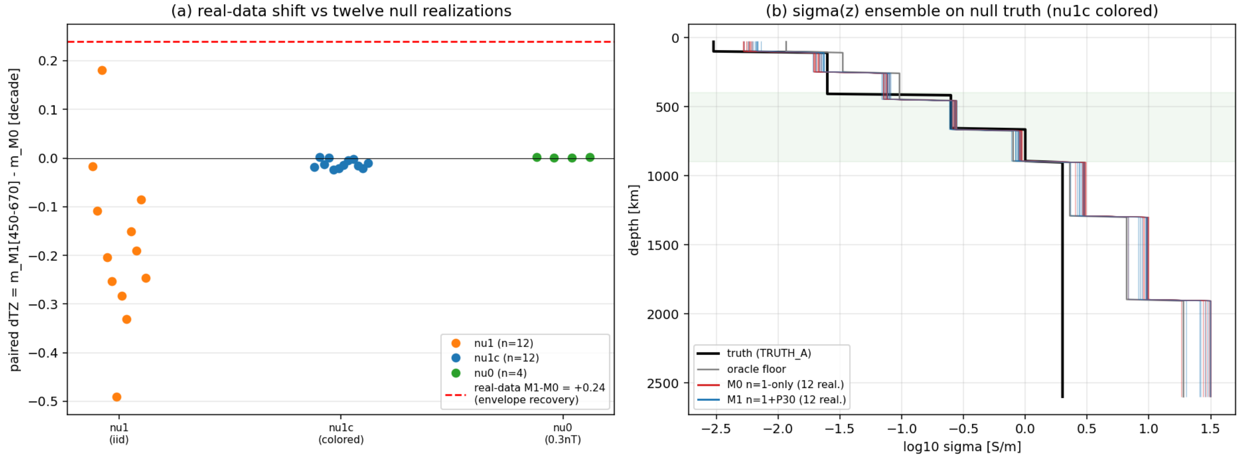
(a) real-data shift vs twelve null realizations

(b) sigma(z) ensemble on null truth (nu1c colored)

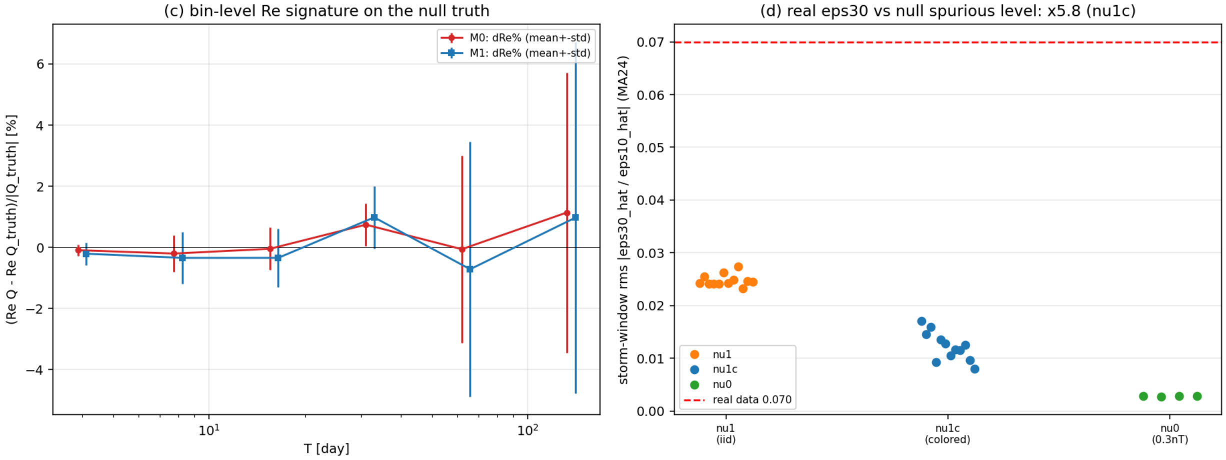
(c) bin-level Re signature on the null truth

(d) real eps30 vs null spurious level: x5.8 (nu1c)

Fig. S2. null synthetic — paired ΔTZ under three noise families; σ(z) ensemble at the oracle floor; spurious-amplitude floor.

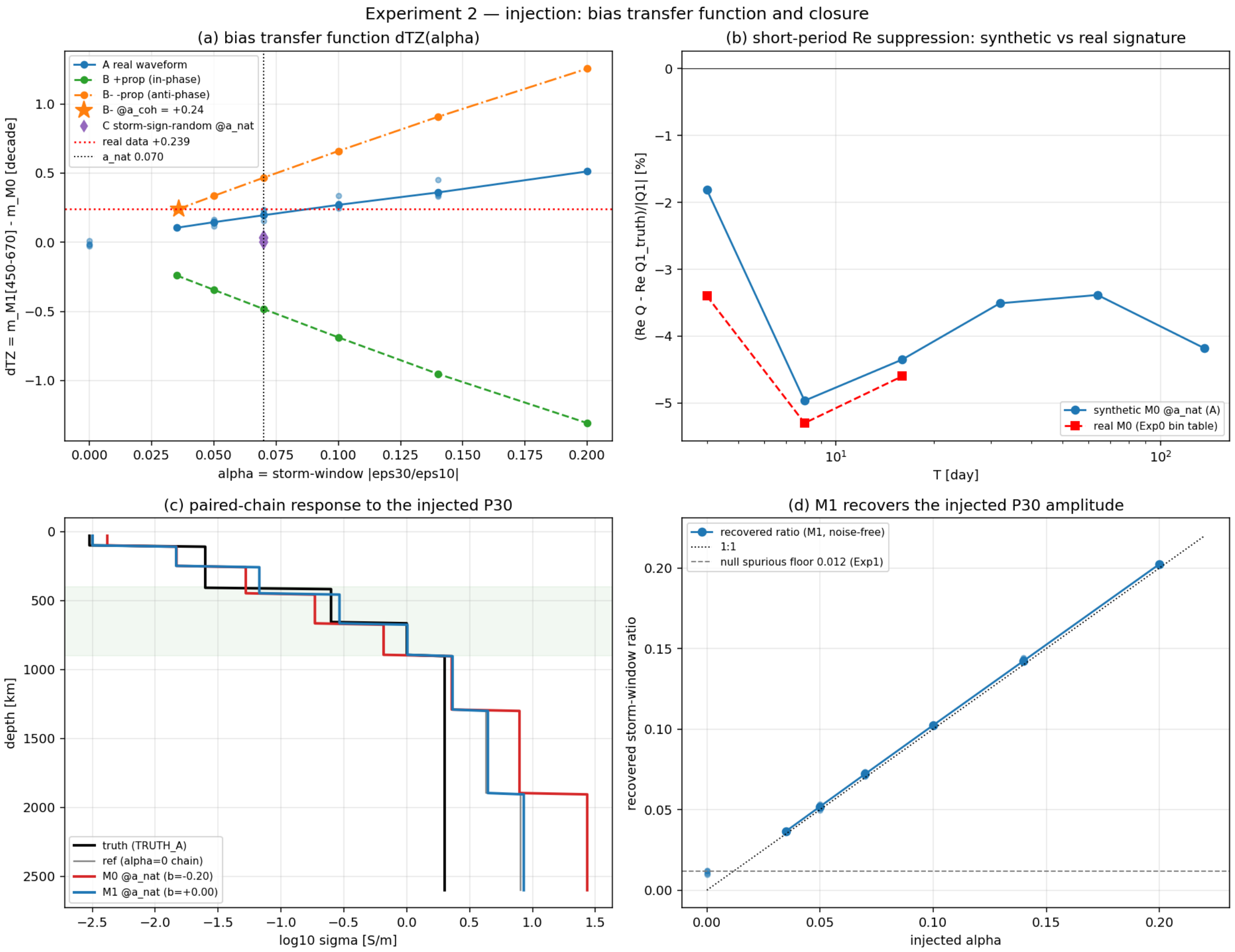

Fig. S3. injection experiments — full transfer functions, recovery, signatures.

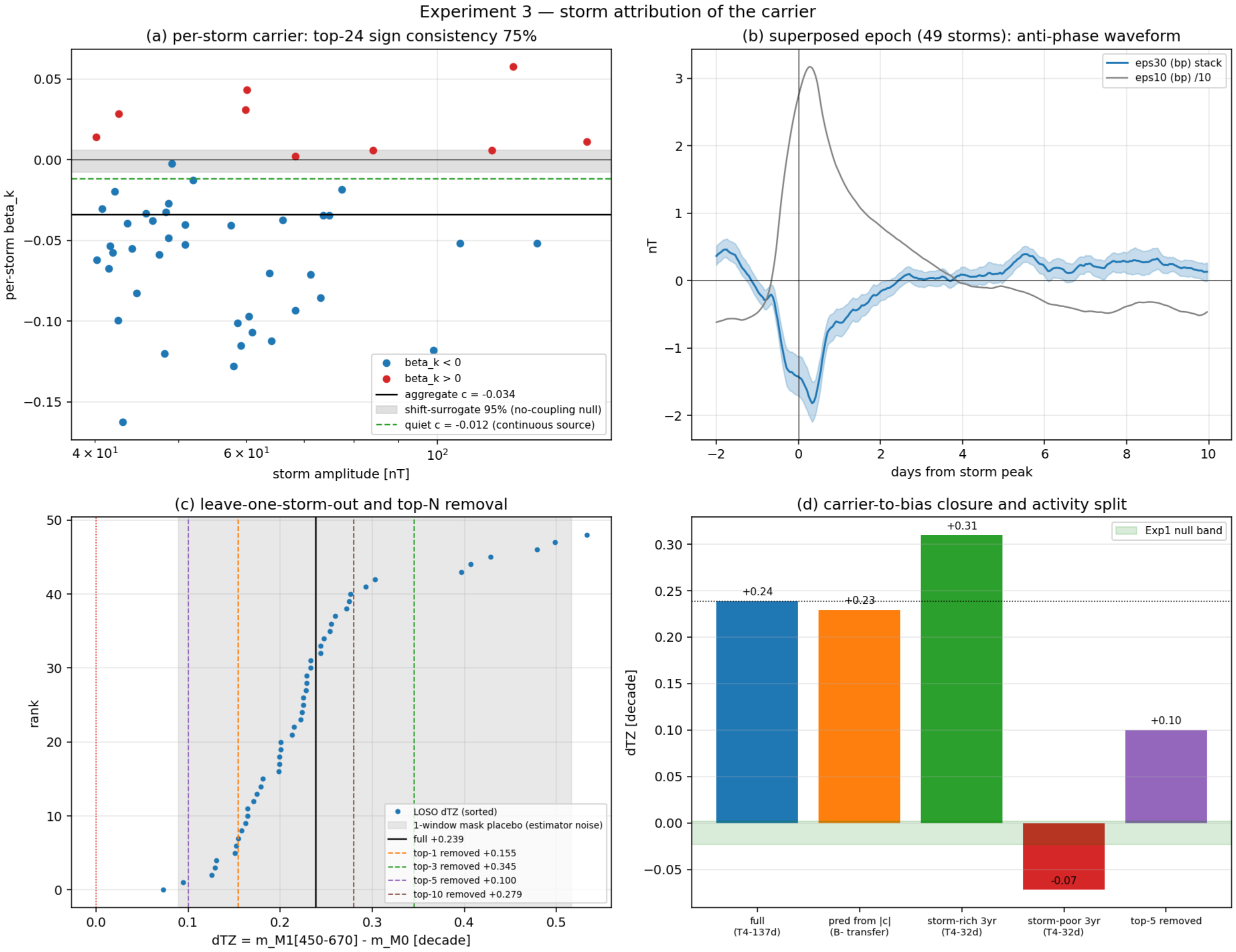

Fig. S4. per-storm carrier, surrogate bands, LOSO and top-N with mask placebo, year split, prediction closure.

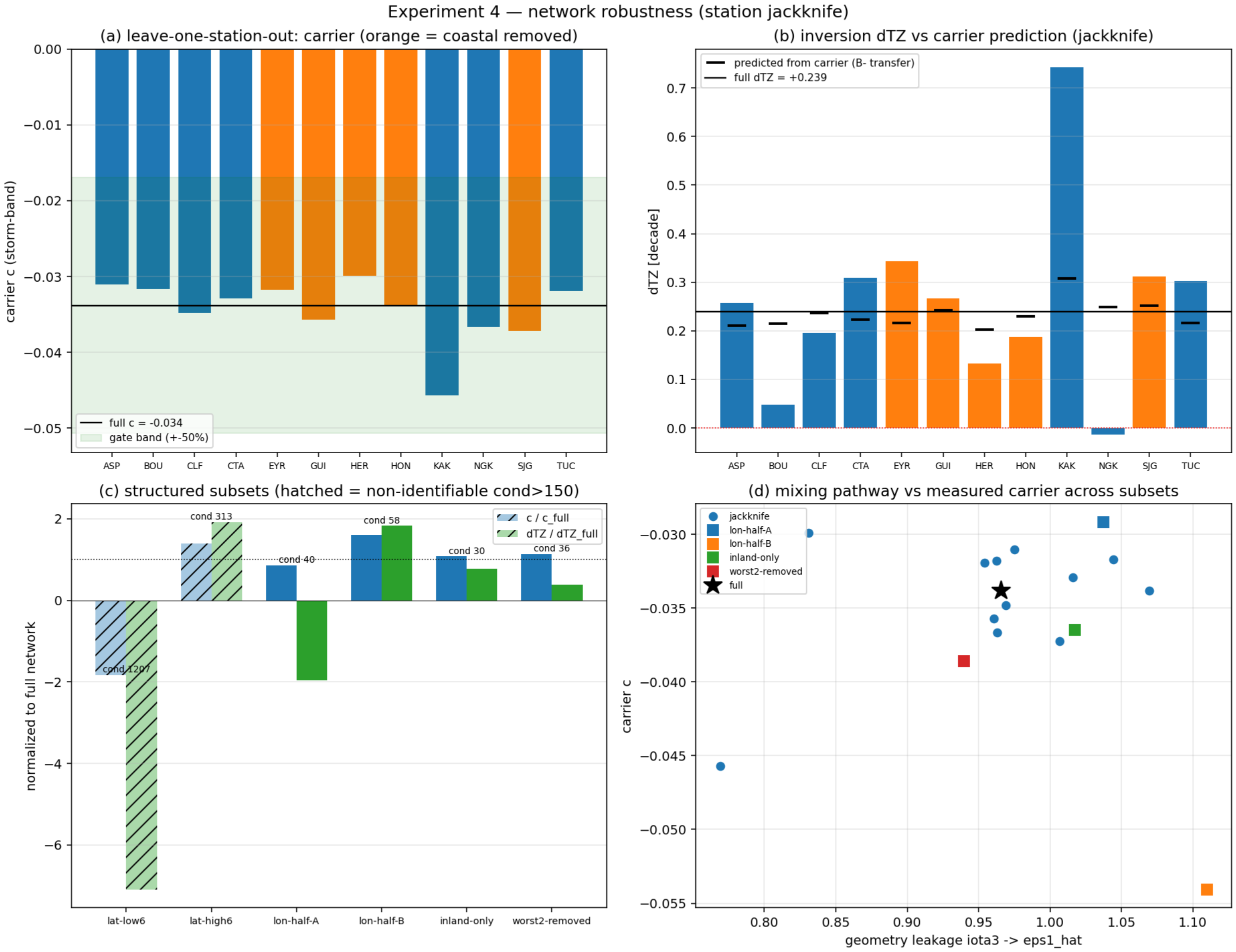
Experiment 4 — network robustness (station jackknife)

(a) leave-one-station-out: carrier (orange = coastal removed)

(b) inversion dTZ vs carrier prediction (jackknife)

(c) structured subsets (hatched = non-identifiable cond>150)

(d) mixing pathway vs measured carrier across subsets

Fig. S5. station jackknife and structured subsets; identifiability (latitude leverage).

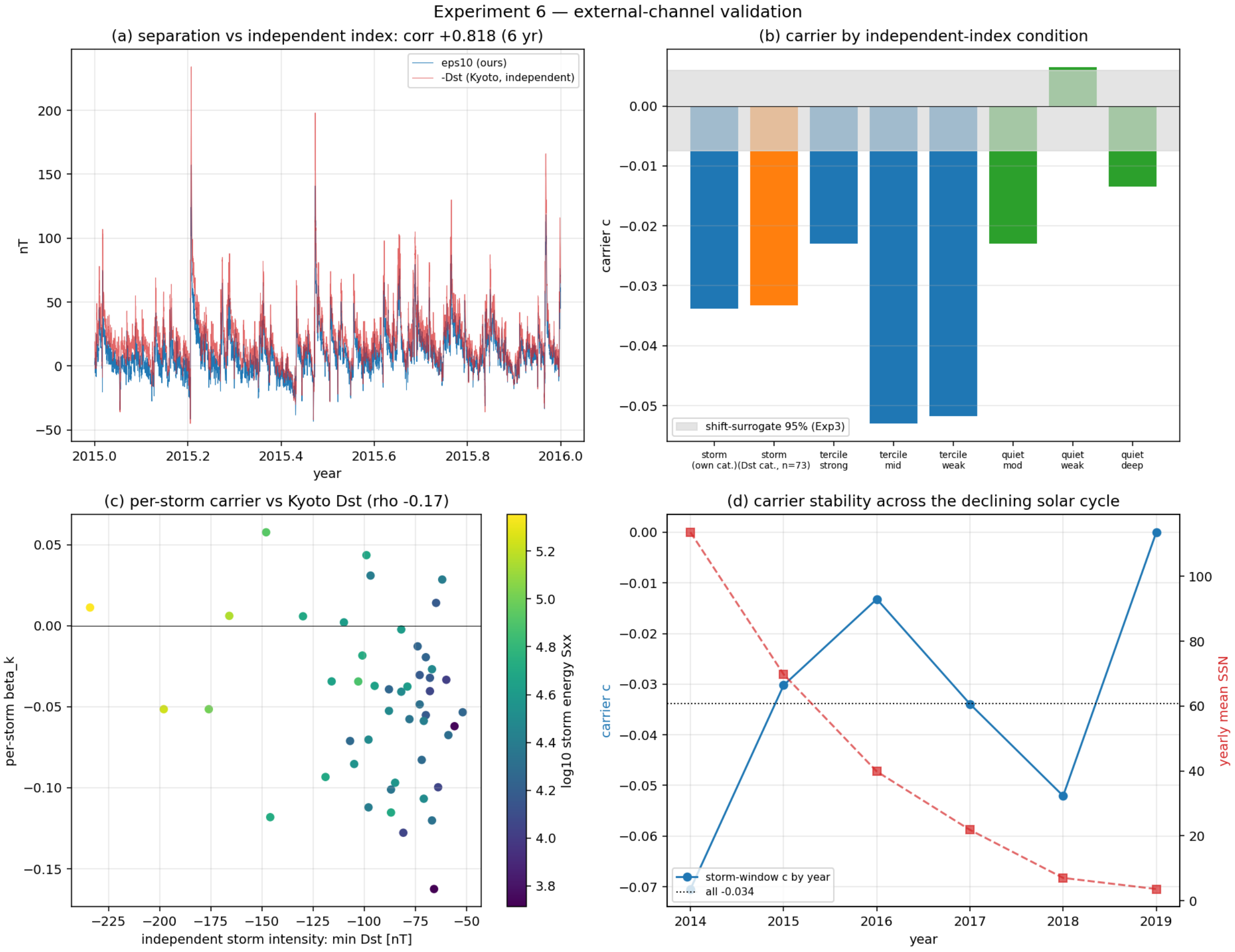

Fig. S6. independent-index validation; quiet stratification; per-storm β versus Dst; yearly carrier.

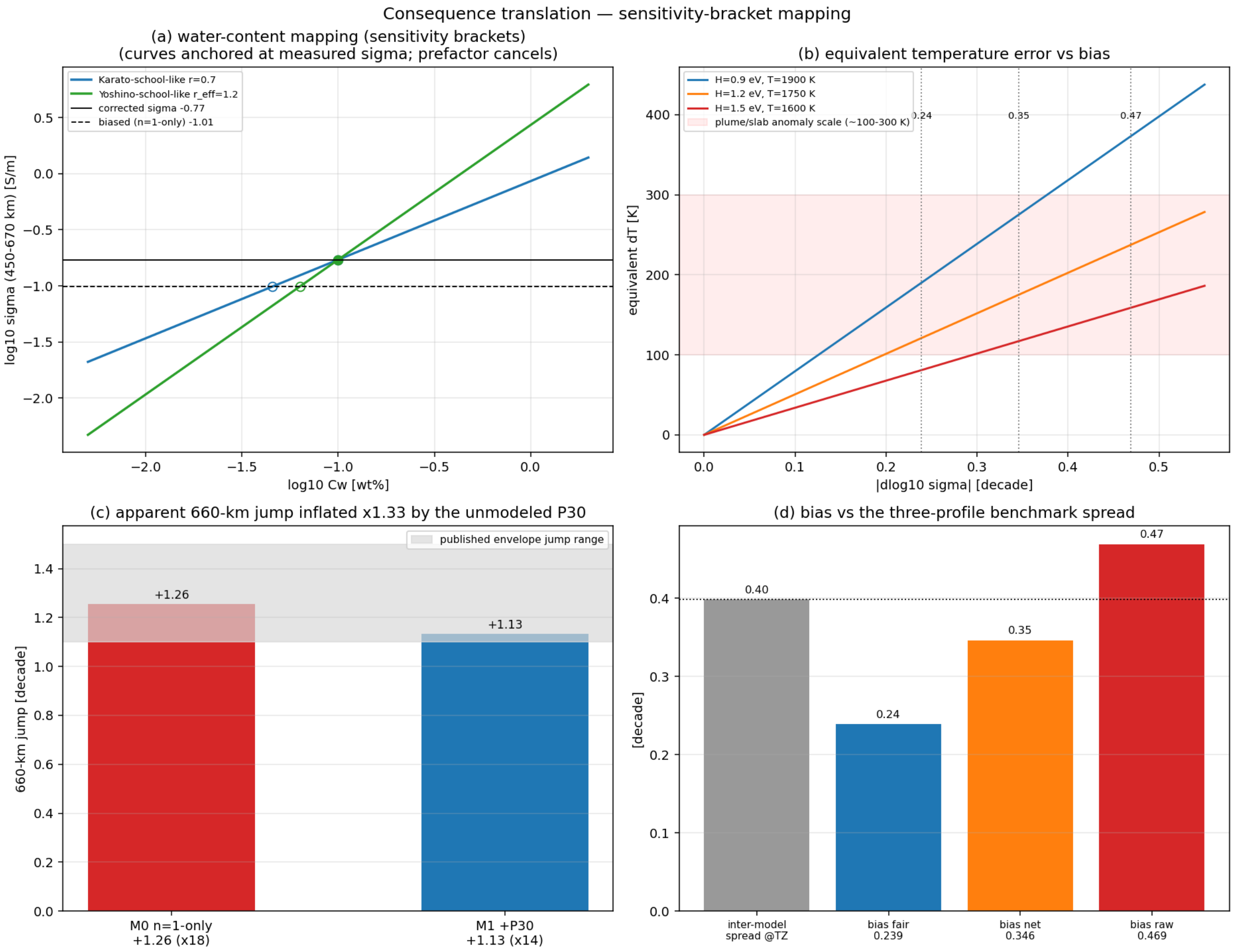

Fig. S7. translation details behind Fig. 5.

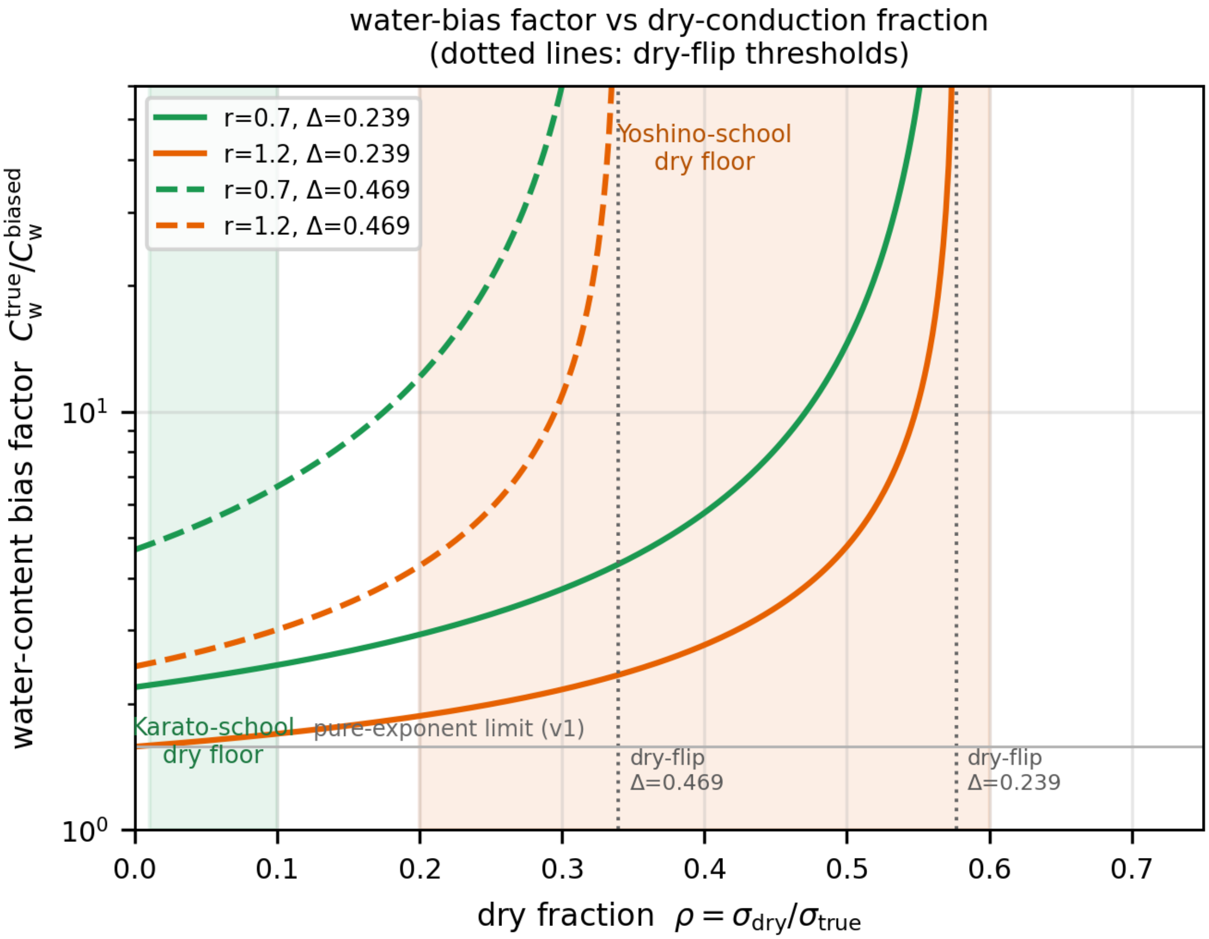

Fig. S8. dry-floor-corrected water-bias factor F(ρ) for both laboratory-school regimes; dry-flip thresholds (§S9 v2).

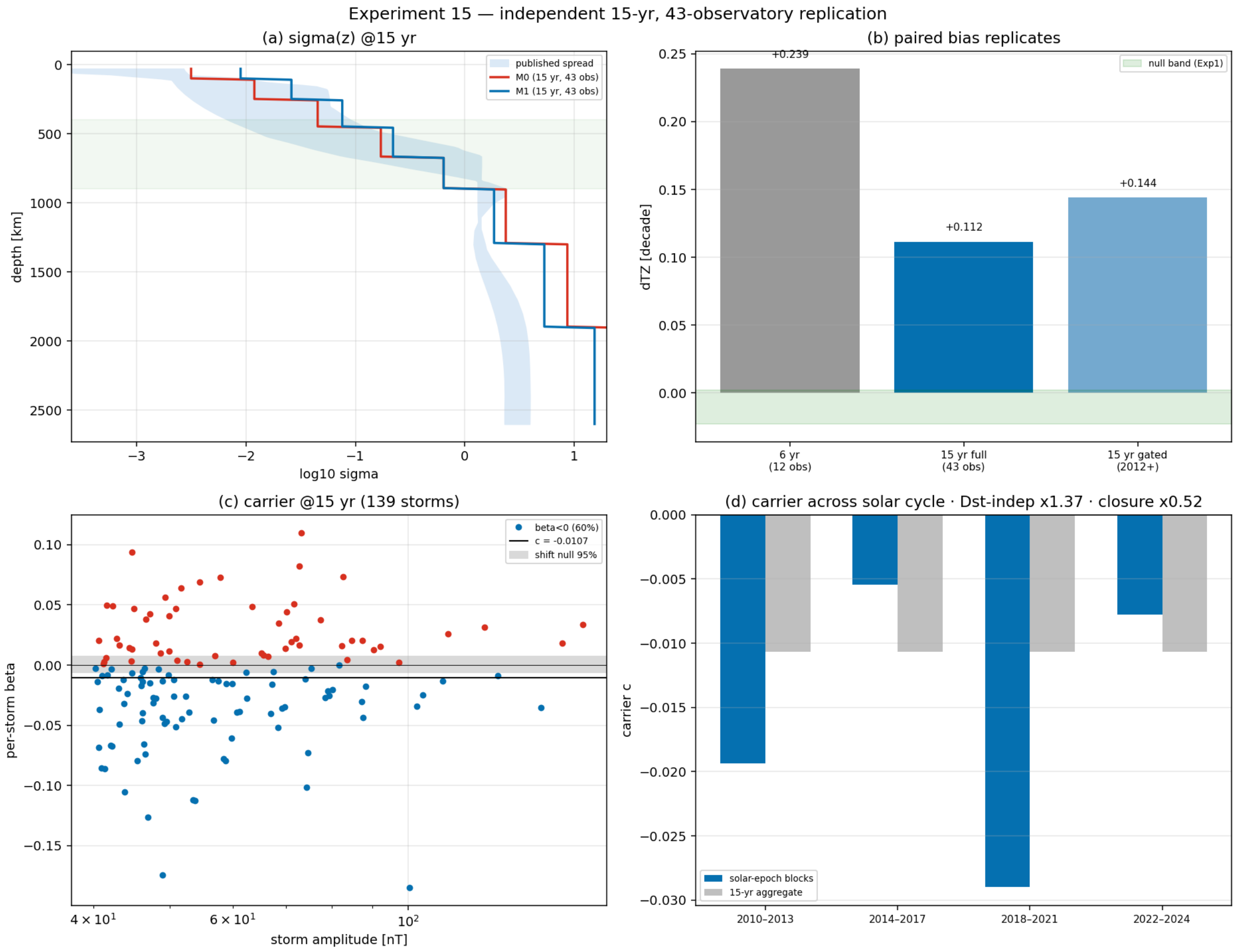

Fig. S9. 15-yr, 43-station replication panels (§S11).

Table S1. Source-model configurations (single run, identical pipeline)

Config	basis	n_coef	cond	χ^2/n	envelope dist.	excess over floor	660 jump
M0	n=1 (m≤1)	6	20.3	0.25	0.377	+0.248	+1.26
M1	**+ (3,0)**	8	35.6	0.46	**0.200**	**+0.071**	+1.13
M2	+ (3,0),(3,±1)	12	1283.9	1.07	0.731	+0.601	+1.54
M3	+ (3,0),(5,0)	10	199.8	1.05	1.686	+1.557	+1.17
Mbad1–3	+ shuffled (3,0)	8	28.6–29.3	0.17–0.33	0.352–0.468	+0.22–+0.34	+1.24–+1.28
M0 (discovery band)	n=1, T≥2 d	6	20.3	0.97	0.469	+0.346	+1.33

Machine floor (adopted band): per-anchor 0.098/0.129/0.255, median 0.129.

Table S2. Gate ledger

Gate	criterion (final)	outcome	revision
E0a–E0f	lock: self-check, provenance ×2, keystone, shuffled control, escalation	6/6 PASS	—
E1a–E1c	null sanity / real-outside-null / no-win	3/3 PASS	(1)(2) §S10
E2a–E2d	injection recovery / monotone / closure CLOSED / immunity	PASS+CLOSED	(3)
E3a–E3c	carrier real·sign / shift-null + enhancement + year split / no single event	3/3 PASS	(4)(5)
E4a–E4c	jackknife carrier / inland-only / structured sign	3/3 PASS	(6)
E6a–E6c	index corr ≥0.7 / independent catalog ×0.5–2 / AE	PASS·PASS·SKIP	—

Table S3. Storm catalogs

Self-detected: 49 events ($\hat{\varepsilon}_1^0$ peaks ≥40 nT, ≥5-day separation), 2014–2019; top five (2015-03-17 St. Patrick; 2015-06-23; 2015-12-20; 2018-08-26; 2017-09-08) all match known storms at correct absolute times. Dst-independent: 73 events (min Dst < −50 nT); window overlap with self-detected 66%. Full event lists are provided in the data deposit (doi:10.5281/zenodo.21184326).

Table S4. Observatories

Code	|maglat| (°)	coastal	availability
ASP, BOU, CLF, CTA, KAK, NGK, TUC	22–52 (inland 7)	no	93–100%
EYR, GUI, HER, HON, SJG	(coastal 5)	yes	79–100% (SJG 79%)

Per-observatory IAGA codes are listed in the tables above; precise coordinates, operating institutes, and the standard INTERMAGNET and World Data Centre data-provider acknowledgments accompany the archived station metadata in the deposit.

Table S5. Consequence translation (sensitivity-bracket method)

$\Delta\log_{10}\sigma$	water factor (r 1.4→0.6)	ΔT (K)	context
0.239 (fair)	×1.5–2.5	81–190	keystone band
0.346 (net, floor-corrected)	×1.8–3.8	117–275	discovery band net
0.469 (raw)	×2.2–6.0	159–373	headline upper bound

660-km jump: +1.26 → +1.13 decades (apparent contrast ×18.0 → ×13.6; ×1.33 inflation; published-model jump range +0.90 to +1.94 — both within). Published TZ spread (§S2a): 1.27 decades; bias = 19% (fair), 27% (net), 37% (raw).

Table S6. Source treatment in representative long-period induction chains

Classification protocol: **VV** = verbatim quotation secured from the original text; **V** = unambiguous from title/abstract. All rows were verified against the original sources. Self-correction on record: Olsen (1998) and Olsen (1999), provisionally classed P10-based, were both *refuted* on reading the originals (Z:Y method; global spherical-harmonic analysis) and reclassified as source-aware – the protocol that grounds this table.

Chain	Data / band	Source treatment (magnetospheric channel)	Class	Status
Banks 1969 (15)	obs, Dst band	P_1^0 dominance established; responses via P_1^0	P_1^0-response	**VV**
Schultz & Larsen 1987 (40)	global obs	scalar response collection under P_1^0	P_1^0-response	**VV**
Olsen 1998 (17)	Europe obs, 3–720 h	**Z:Y method; monthly SHA, n ≤ 10 (damped)**	source-aware	**VV**
Olsen 1999 (18)	Europe obs, 30 d–1 yr	long-period C-responses (Z:Y global SHA)	source-aware	**VV**
Fujii & Schultz 2002 (41)	global obs	3-D response to ring current + auroral oval	source-structure diagnosis	**V**
Utada 2003 / Shimizu 2010 (42, 43)	N-Pacific semi-global	C-responses	P_1^0-response	**VV**
Kuvshinov & Olsen 2006 (8)	CHAMP/Ørsted/SAC-C	Dst-parameterized external q_1^0	P_1^0-response	**VV**
Balasis & Egbert 2006 (19)	obs EOF	non-axisymmetric source evidence	diagnosis	**V**
Kelbert et al. 2009 (9)	global obs → 3-D	C/Q-responses at observatories	P_1^0-response	**VV**
Velímský 2010 (27)	CHAMP, time domain	external degree-1 forcing	P_1^0-response	**V**

Chain	Data / band	Source treatment (magnetospheric channel)	Class	Status
Semenov & Kuvshinov 2012 (10)	global obs → 3-D	corrected C-responses	P_1^0-response (corrected)	**VV**
Sun, Kelbert & Egbert 2015 (39)	global obs	ionospheric + magnetospheric source co-modeling	source-aware	**V**
Püthe, Kuvshinov & Olsen 2015 (20)	methodology	transfer functions for complex sources	source-aware (method)	**V**
Püthe et al. 2015 (11)	satellite+obs → 1-D	**“single spherical harmonic Y_1^0” (verbatim)**	**P_1^0-response**	**VV**
Civet et al. 2015 (12)	Swarm → 1-D	external degree-1	P_1^0-response	**VV**
Grayver et al. 2017 (13)	satellite (C1+tidal) → 1-D	**“only the term corresponding to n=1, m=0 was used to estimate C1-responses” (manuscript verbatim)**	**P_1^0-response (magnetospheric channel)**	**VV**
Munch et al. 2018 (26)	obs → 1-D	C-responses, ocean-effect treatment	P_1^0-response	**VV**
Guzavina et al. 2019 (49)	obs, Sq band	global-to-local TFs (non-P_1^0 channel)	source-aware (Sq)	**V**
Zhang et al. 2022 (45)	obs, Sq diurnal → TZ	ionospheric source modeling	source-aware (Sq)	**V**

Reading. Source-aware methodology has existed since 1998 in a parallel lineage (Z:Y analysis; EOF diagnosis; complex-source transfer functions; ionospheric co-modeling; Sq channels). The standard 1-D *profile products*, however — the chains whose disagreement spans a representative published spread (§S2a) — estimate their magnetospheric responses on the P_1^0 assumption, **verbatim- verified for both flagship models compared in this work** (11, 13). The main-text claim is calibrated to this table: the exposed population is the P_1^0-response lineage, classified per paper against the original sources (verbatim where quoted; see the VV/V flags).

§S12. AI-use disclosure (scope of use)

In accordance with the Science journals’ editorial policy on AI-assisted technologies, we disclose the following. An AI assistant (Claude, Anthropic; Claude Opus 4-series models, used interactively through the Claude Code environment, 2026) was used, under the author’s direction, to assist with batch-script preparation, log summarization, bibliographic metadata checking, and language editing of the manuscript and Supplementary Materials. The AI system did not determine the research questions, experimental design, acceptance criteria, data selection, statistical interpretation, scientific conclusions, or authorship. All analyses were executed from deposited scripts and locked intermediate files; all numerical results, figures, references, and interpretations were independently checked and approved by the author, who takes full responsibility for the integrity and accuracy of the work. All figures are deterministic renderings of the locked data archives by the deposited plotting scripts; no generative-AI imagery is used anywhere in the manuscript or Supplementary Materials. No output of the AI system entered the manuscript without author verification, and no AI system is listed as an author. This disclosure is repeated in the Acknowledgments and in the cover letter.

References and Notes (continued from main text)

32. R. L. Parker, The inverse problem of electromagnetic induction: existence and construction of solutions based on incomplete data. *J. Geophys. Res.* **85**, 4421–4428 (1980). doi:10.1029/jb085ib08p04421
33. P. Weidelt, The inverse problem of geomagnetic induction. *Z. Geophys.* **38**, 257–289 (1972).
34. S. C. Constable, R. L. Parker, C. G. Constable, Occam's inversion: a practical algorithm for generating smooth models from electromagnetic sounding data. *Geophysics* **52**, 289–300 (1987). doi:10.1190/1.1442303
35. C. L. Lawson, R. J. Hanson, *Solving Least Squares Problems* (SIAM Classics, 1995; orig. 1974). doi:10.1137/1.9781611971217
36. P. Welch, The use of fast Fourier transform for the estimation of power spectra: a method based on time averaging over short, modified periodograms. *IEEE Trans. Audio Electroacoust.* **15**, 70–73 (1967). doi:10.1109/tau.1967.1161901
37. C. T. Russell, R. L. McPherron, Semiannual variation of geomagnetic activity. *J. Geophys. Res.* **78**, 92–108 (1973). doi:10.1029/ja078i001p00092
38. C. Kloss, chaosmagpy: evaluation software for the CHAOS geomagnetic field model, Zenodo. doi:10.5281/zenodo.3352398
39. J. Sun, A. Kelbert, G. D. Egbert, Ionospheric current source modeling and global geomagnetic induction using ground geomagnetic observatory data. *J. Geophys. Res. Solid Earth* **120**, 6771–6796 (2015). doi:10.1002/2015jb012063
40. A. Schultz, J. C. Larsen, On the electrical conductivity of the mid-mantle — I. Calculation of equivalent scalar magnetotelluric response functions. *Geophys. J. R. Astron. Soc.* **88**, 733–761 (1987). doi:10.1111/j.1365-246x.1987.tb01654.x
41. I. Fujii, A. Schultz, The 3D electromagnetic response of the Earth to ring current and auroral oval excitation. *Geophys. J. Int.* **151**, 689–709 (2002). doi:10.1046/j.1365-246x.2002.01775.x
42. H. Utada, T. Koyama, H. Shimizu, A. D. Chave, A semi-global reference model for electrical conductivity in the mid-mantle beneath the north Pacific region. *Geophys. Res. Lett.* **30**, 1194 (2003). doi:10.1029/2002gl016092
43. H. Shimizu, T. Koyama, K. Baba, H. Utada, Revised 1-D mantle electrical conductivity structure beneath the north Pacific. *Geophys. J. Int.* **180**, 1030–1048 (2010). doi:10.1111/j.1365-246x.2009.04466.x
44. A. Khan, A. Kuvshinov, A. Semenov, On the heterogeneous electrical conductivity structure of the Earth's mantle with implications for transition zone water content. *J. Geophys. Res.* **116**, B01103 (2011). doi:10.1029/2010jb007458
45. H. Zhang, G. D. Egbert, Q. Huang, A relatively dry mantle transition zone revealed by geomagnetic diurnal variations. *Sci. Adv.* **8**, eabo3293 (2022). doi:10.1126/sciadv.abo3293
46. [dataset] A. V. Grayver, Reference conductivity profile of the mantle (agrayver/ConductivityProfile; repository for ref. 13), Zenodo (2020). doi:10.5281/zenodo.4058852
47. [dataset] IRIS EMC, GlobalEM-2009-10×10 (global electromagnetic induction constraints on

transition-zone water content; 3-D conductivity model of ref. 9), Incorporated Research Institutions for Seismology (2019). doi:10.17611/DP/GLOBALEM200910X10

48. [dataset] IRIS EMC, GlobalEM-2015-02×02 (high-resolution global mantle conductivity from ground observatory data; 3-D conductivity model of ref. 39), Incorporated Research Institutions for Seismology (2019). doi:10.17611/DP/GLOBALEM201502X02
49. M. Guzavina, A. Grayver, A. Kuvshinov, Probing upper mantle electrical conductivity with daily magnetic variations using global-to-local transfer functions. *Geophys. J. Int.* **219**, 2125–2147 (2019). doi:10.1093/gji/ggz412

Data and code availability

INTERMAGNET definitive data (29); WDC-Kyoto final Dst (23); SILSO sunspot number (31); CHAOS-7 (30). All processing and experiment code, the locked intermediate artifacts (`exp0…exp6`, `consequence_translation`, Kyoto cache, century-import layer archives behind Fig. 4), and the gate ledger regenerate every figure deterministically in seconds; the deposit is archived at Zenodo (doi:10.5281/zenodo.21184326). The deposit manifest additionally includes, for the century-archive import of §S11: the era-gated chain code, the observatory selection list, the paired A/B and 20-draw envelope outputs (`gds_p30_bias`, `gds_p30_sweep`, `gds_p30_sweep_env`), and the reproduction guide documenting chain construction, era gates, and admission diagnostics — sufficient to re-derive every century number quoted in this paper from the deposit alone.